이학박사 학위논문

Accurate determination of the thermoelectric properties of suspended Bi_2Se_3 epifilms with varied thickness

현수 구조의 Bi_2Se_3 박막의 두께에 따른 열전 효과의 변화 정밀 측정

2023년 2월

서울대학교 대학원

물리천문학부

김동욱

Accurate determination of the thermoelectric properties of suspended Bi_2Se_3 epifilms with varied thickness

Donguk Kim

Supervised by
Professor Yun Daniel Park

A dissertation submitted to the Faculty of Seoul National University in Partial Fulfillment of the Requirements for the Degree of Doctor of Philosophy

February 2023

Graduate School of
Department of Physics and Astronomy
Seoul National University

Physics Major

Accurate determination of the thermoelectric properties of suspended Bi_2Se_3 epifilms with varied thickness

현수 구조의 Bi_2Se_3 박막의 두께에 따른 열전 효과의 변화 정밀 측정

지도교수 박 윤

이 논문을 이학박사 학위논문으로 제출함
2022년 12월

서울대학교 대학원
물리천문학부
김 동 욱

김동욱의 이학박사 학위논문을 인준함
2022년 12월

위 원 장 이 진 호 (인)

부위원장 박 윤 (인)

위 원 김 도 헌 (인)

위 원 장 준 호 (인)

위 원 고 태 준 (인)

Abstract

This dissertation describes experimental studies on the measurement of the thermoelectric (TE) effect of molecular beam epitaxially (MBE) grown Bi_2Se_3 on GaAs (111)A substrate. Nanostructuring can enhance the thermoelectric efficiency by effectively reducing thermal conductivity. The accurate measurement of the thermal conductivity of Bi_2Se_3 thin films is challenging due to substrate heat diffusion. The Bi_2Se_3 samples are suspended using a nanomachining technique, namely, the selective wet etching of GaAs buffer/substrate layer by citric acid solution followed by a critical point drying method to prevent structural collapse owing to the surface tension of the liquid. This thermally isolates the Bi_2Se_3 sample from the GaAs substrate. Furthermore, the self-heating 3ω method is utilized to accurately measure the thermal conductivity of the suspended Bi_2Se_3. The sputtered Pt elements serve as local Joule heaters, thermometers, and voltage probes for determining the Seebeck coefficient. The thermal conductivity, the electrical conductivity, and the Seebeck coefficient are measured simultaneously using the incorporated electrical Pt probes in a cryostat system in the temperature range of 60-300K.

The MBE growth procedures of Bi_2Se_3 are optimized by scanning the parameters. First, the GaAs buffer layer determines the roughness and surface defects of the substrate. The grown GaAs buffer layer/GaAs (111)A is scanned using atomic force microscopy (AFM) and the resultant image indicates that a 40 nm-thick

buffer layer can reduce the surface roughness and defects. Second, the growth temperature and growth rate of Bi_2Se_3 are examined. Using the optimized growth conditions, Bi_2Se_3 thin film is grown from a thickness of 20 nm to 300 nm by controlling the growth time. The thickness is determined by the growth rate and growth time. The growth rate of Bi_2Se_3 depends on the flux of Bi and increases linearly with it. The growth temperature, flux ratio between Bi and Se, and buffer layer do not affect the thickness of Bi_2Se_3. All the grown Bi_2Se_3 are fabricated to form a suspended device, but the films thinner than 100 nm are structurally unstable to the vibrations caused by the compressor of the cryostat. Only the case of 150, 200, and 300 nm Bi_2Se_3 are measured and presented in this dissertation. The thermal conductivity, electrical conductivity, and absolute value of the Seebeck coefficient are decreasing with the thickness. The TE figure of merit (*ZT*) at room temperature is the highest for a sample of whose thickness is 200 nm.

Keywords : molecular beam epitaxy (MBE), Bi_2Se_3, thermoelectric effect, 3ω method, nanomachining.

Student Number : 2018-21337

Table of Contents

Lists of Figures

Chapter 1. Introduction

1.1. Thermoelectric effect

Recently, interest in renewable energy has increased owing to global warming caused by CO_2 emission that pollutes the air and leads to rapid climate change. Many countries are focusing on the development of sustainable green energy, including carbon-free power generation such as solar, wind, biogas, and hydro energy as well as techniques for reusing waste heat. Considering Joule heating, most energy is converted to heat after working. However, in the case of automobiles, only 15% of the energy is reused for driving and refrigeration, while the remaining 85% is discarded as heat energy. Currently, the ratio of recycled to discarded heat is extremely low. Hence, thermoelectric (TE) devices that can convert thermal energy into useful electrical energy are considered futuristic and are being rapidly developed. TE devices are used in the automobile, aerospace, semiconductor, optics, computer, power generation, and electric product industries. TE devices are indeed beneficial because they are applicable to both renewable energy and energy generation as the electrical voltage is generated by geothermal sources, heat from the sun, and even

by the human body. In particular, the heat from the human body can generate electricity through a TE device, which gives rise to the idea of a wearable device that monitors the medical condition of the body. The TE device is maintenance-free and semi-permanent because it produces electricity from heat without any moving parts. Hence, TE is also applicable to spacecraft. Wider application of TE devices will be possible if the efficiency of energy conversion increases.

The efficiency of TE devices is described by the figure of merit (ZT). Higher ZT values indicate better energy conversion efficiency. The value of ZT either can be determined analytically or experimentally. The experimental method may be indirect (by measuring each TE property that impacts ZT) or direct (by measuring ZT). Although the field of TE devices has advanced since the 1950s, little progress was made in increasing ZT. Although a high ZT of 2.5 has been reported from Bi_2Te_3/ Sb_2Te_3 superlattices, most studies demonstrate that the upper limit of ZT is approximately 1. Owing to technological development, ZT can be estimated by computational or numerical methods. Theoretical studies of TE materials indicate the possibility of enhancing the ZT by more than twice the experimentally measured value. At present, most commercial TE devices use Bi_2Te_3-based alloys, but the scarcity and toxicity of Tellurium require the development of cost-effective Se-based TE materials such as Bi_2Se_3 or Bi_2Se_3-based alloys.

1.2. 3ω method

Thin films, superlattices, graphene, and other 2-D materials are studied in various branches including memory, optics, and TE effects. Thermal performance is very important in many of these studies. The thermal conductivity of thin films is usually smaller than that of bulk materials. In this study, the thermal conductivity of a 200 nm-thick Bi_2Se_3 film is two times smaller than that of bulk Bi_2Se_3, as reported elsewhere.

In the case of DC heating to measure the thermal conductivity, the temperature may be determined in a straightforward manner from measurements of the current and voltage of the heater and its R-T curve. However, in the case of AC current at an angular frequency ω, 2ω Joule heating is induced. Owing to the linear response in the thermal domain, the 2ω heating causes temperature fluctuations at 2ω. This temperature fluctuation depends on the thermal properties of the material such as thermal conductivity and heat capacity. Considering Ohm's law, the driving AC current at ω with the temperature fluctuation at 2ω will induce 3ω voltage. Hence, the thermal conductivity can be determined by measuring the 3ω voltage.

The 3ω method has several advantages over DC measurements. First, the measurement is insensitive to the boundary condition between the substrate and the environment. Assuming that the thermal diffusivity of the substrate is a few times smaller than the substrate thickness, the thermal fluctuation is localized within the substrate, and thus, the AC thermal response is insensitive to the boundaries. However, the thermal wavelength increases with decreasing frequency. In the limit of zero frequency, namely, DC current, the thermal fluctuation depends on the

boundary conditions. In addition, AC measurements can reduce the substrate contribution, DC voltage artifacts from the TE effect, and low-frequency drifts.

In the case of films on a substrate, determining the lateral thermal conductivity requires measurements of the vertical thermal conductivity because the substrate effect is not negligible. However, the substrate effect can be ignored by suspending the material from the substrate, and the 3ω method directly provides information regarding thermal conductivity. As mentioned above, the material itself is heated up by the driven DC current to induce 3ω voltage. This method, which is called the self-heating 3ω method, is known to be accurate because measurements of vertical thermal conductivity are not required.

1.3. Molecular beam epitaxy

Molecular beam epitaxy (MBE) is an epitaxy method that is frequently used for the thin-film deposition of single crystals. MBE that had been widely adapted to growth since 1970s is suitable for atomic-level deposition as the name connoted. Hence, the accurate control of doping level makes it suitable for growing thin semiconductor films. MBE is a carefully and accurately controlled form of vacuum evaporation. Effusion cells for evaporation create beam flux of atoms individually in an ultrahigh vacuum (UHV) environment. The UHV (where the pressure is below 10^{-9} Torr), is essential for reducing the impurity levels in the growing layers. The growth conditions in the environment and accurate control of the sources allow higher grown film purity and quality than other growth techniques although the long cooling time by liquid nitrogen gas and low deposition rate result in comparatively lower yields. The schematic of the MBE system is shown in Figure 1.1. The MBE

system consists of a stainless-steel chambers that are named as load lock, prebake, transfer and main (growth) chamber, respectively. These chambers are connected each other by gate valves to minimize contamination of environment (lab), components and materials sources. The system maintains pressure as low as possible by the following pumping system. Each chamber is maintained at UHV by ion pumps, and the main chamber has additional titanium sublimation pump and LN2 cryopanels. This titanium sublimation pumping can remove residual gas in UHV main chamber since reactive titanium collides with the residual gas and forms a stable, solid product. Thus, the pressures of load lock, prebake and transfer chamber are maintained order of 10^{-8} Torr and the pressure of main chamber is maintained below 10^{-9} Torr. The role of gate valves that isolate each chamber is following. First, the dust and other pollutants from the laboratory environment are evacuated in the load lock chamber. Then, the gate valve between the loading and prebake chambers opens, the sample is moved to prebake chamber to be prebaked. Gate valves isolate the prebake chamber from other chambers. Thus, the contamination from the substrate baking at high temperatures are evacuated at the prebake chamber without affecting on load lock or transfer chamber. Finally, the sample is moved to the main chamber through the clean transfer chamber.

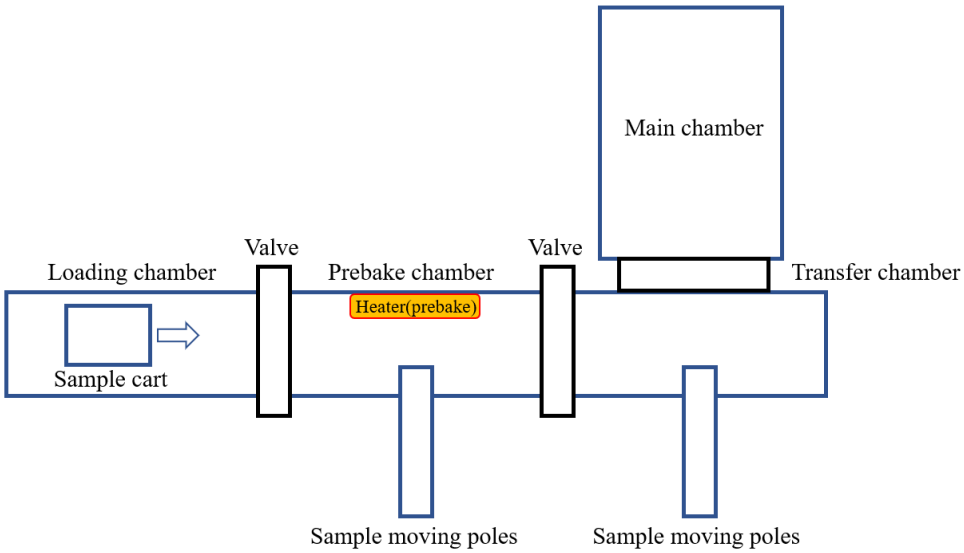

Figure 1.1 Schematic representation of chambers of MBE system.

The main chamber consists of Knudsen effusion cells, reflected high-energy electron diffraction (RHEED), a heater, LN2 cryopanels and other moving parts (sample holder, rotation motor); see Figure 1.2. In addition, titanium sublimation pumping reduces the residual gas pressure of the main chamber. To maintain the UHV condition, a bake (so-called housing) is performed periodically whenever the pressure is not low enough. The bake process is following. The ion pump of the main chamber is turned off and the turbo pump keeps evacuating the entire system. Then, iron plates that are manufactured to be fit onto the main chamber are the heater inside the iron plates heats the entire system to 200 °C. After a few days, the heaters are turned off, the iron plates are disassembled and the ion pump is baked. Finally, the turbo pump is turned off and the ion pump evacuates the main chamber. Under optimum conditions, the pressure of the main chamber is maintained below 10^{-10} Torr.

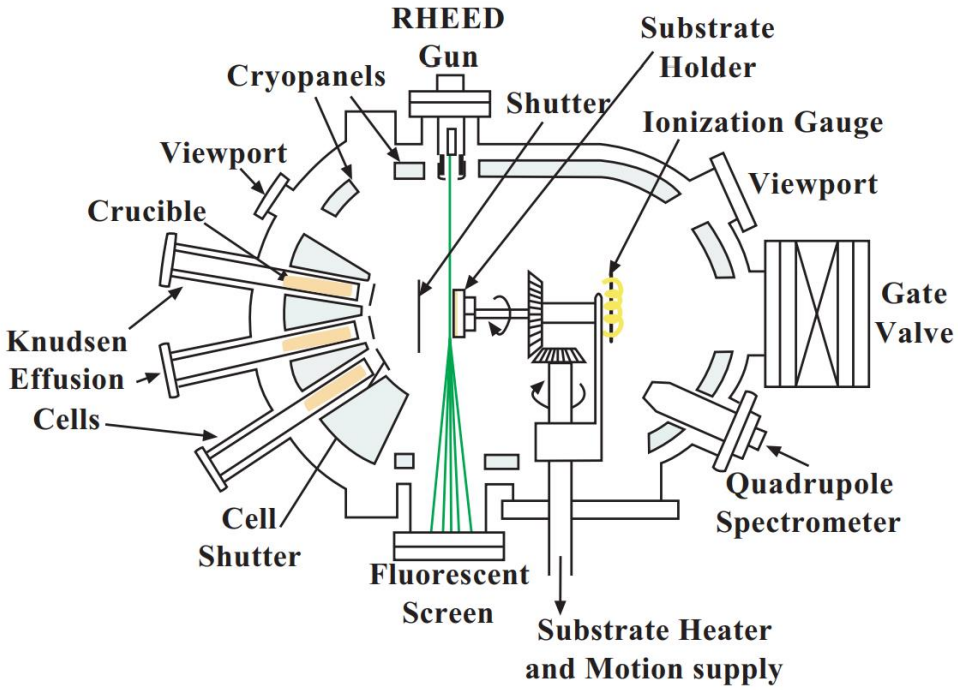

Figure 1.2 Schematic representation of a molecular beam epitaxy growth chamber. The main experimental features component the system is shown [29].

RHEED allows the *in situ* monitoring of thin film growth. The power supply (1.5 A and 12 V) accelerates the electrons so that high-energy electrons are reflected by the surface of the substrate. The RHEED pattern is sensitive to the uppermost layers considering that the incident electron beam collides with the surface in the (almost) parallel direction (angle less than 3°). Then, as shown in Figure 1.3, the reflected beam produces the RHEED patterns. Diffraction from a flat surface produces a high-intensity pattern whereas diffraction from an amorphous surface will produce no diffraction pattern or result in low intensity. Hence, the RHEED pattern provides information about the growth rate and surface features.

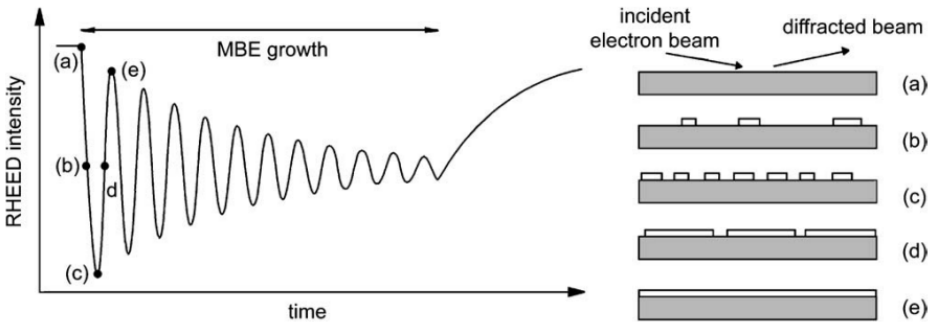

Figure 1.3 Different stages of layer-by-layer growth by nucleation of 2D islands and the corresponding intensity of the zero-order diffracted RHEED beam [30].

A clean substrate is essential for molecular beam epitaxial growth, because the oxidized surface caused by atmospheric exposure results crystal defects that degrade the epitaxial film. So-called "epi-ready grade" wafers are used in MBE growth, this grade wafers are pre-cleaned and oxidized in a controlled environment, to form an oxide layer that can be removed in the MBE chamber. The deoxidation of epi-ready wafers results in consistent and reproducible surface. The growth modes can be classified as layer-by-layer, island, and layer plus island, these modes can be determined by the surface free energy during the growth. For a growth condition with low free energy and large lattice mismatch between the substrate and epifilm, a grown film will have high strain. Hence, even though first a few layer can be grown layer-by-layer, as the thickness increases the top surface forms island to release stress caused by lattice mismatch.

Bi_2Se_3 has a two-dimensional layered rhombohedral crystal structure, in which quintuple layers (QLs) are covalently bonded within the layers but weakly bonded by van der Waals forces between adjacent QLs. This van der Waals epitaxy enables Bi_2Se_3 growth on substrates which have the lattice mismatch of around 15% [31]. The possibility of a wide range of substrates is a highly beneficial for

incorporating topological insulator into devices or studying its optical or electrical properties. Bi_2Se_3 matches the hexagon structure of the GaAs (111)A with a lattice mismatch of 3.55%. The van der Waals epitaxy growth on the substrate with small lattice mismatch results in high quality of crystal structure of Bi_2Se_3 which is introduced in this dissertation.

In this study, the RHEED pattern of deoxidized GaAs (111)A seems streaky without buffer layer. 40 nm-thick GaAs buffer layer is then deposited in order to make the surface better, i.e., low root-mean-square (RMS) roughness and surface defects. Density of surface defects which color is black in the AFM images (Figure 1.5, 1.6, 1.7) decrease as the thickness of GaAs buffer layer increases. With more various studies on buffer layer which are not introduced here, 40 nm thick GaAs buffer layer grown with growth rate of 1 nm/minute is the best film. Here, the growth rate of GaAs buffer layer is determined by controlling the temperature of Ga cell, that is the flux of Ga while the flux ratio between Ga and As is maintained constant.

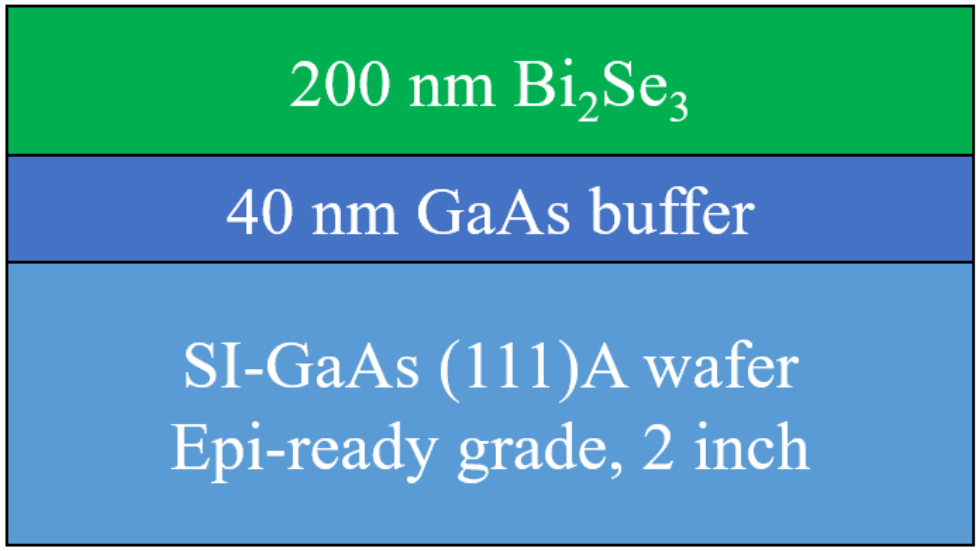

Figure 1.4 Illustration of epitaxial layer sequence and its thicknesses.

From the sequences of growth and AFM scan of Bi_2Se_3 films, the depth of defect is decreasing when the thickness of buffer layer is increasing. The depth measurement is done by choosing some points on the AFM image like in Figure 1.5, 1.6 and 1.7. No differences are found in reflection high-energy electron diffraction (RHEED) pattern and high resolution X-ray diffraction.

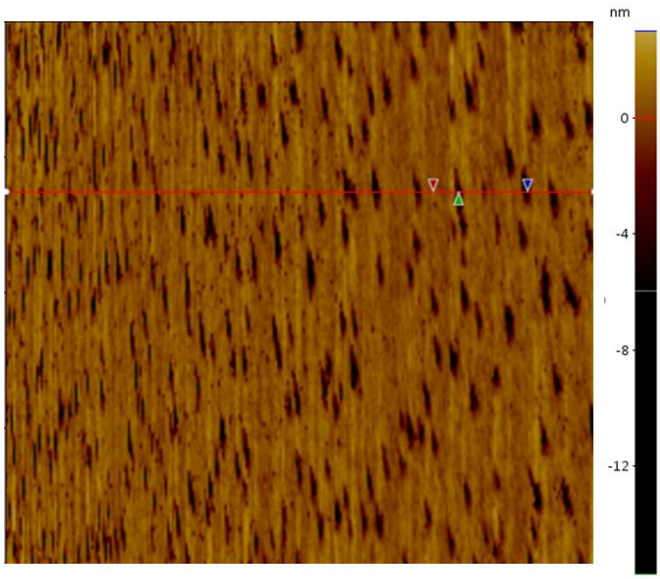

Figure 1.5 AFM scan image of deoxidated GaAs wafer obtained by non-contact mode. The scan area is 1μm×1μm and the height difference (red and green) is 7.4 nm. Root-mean-square (RMS) roughness is 2.5 nm.

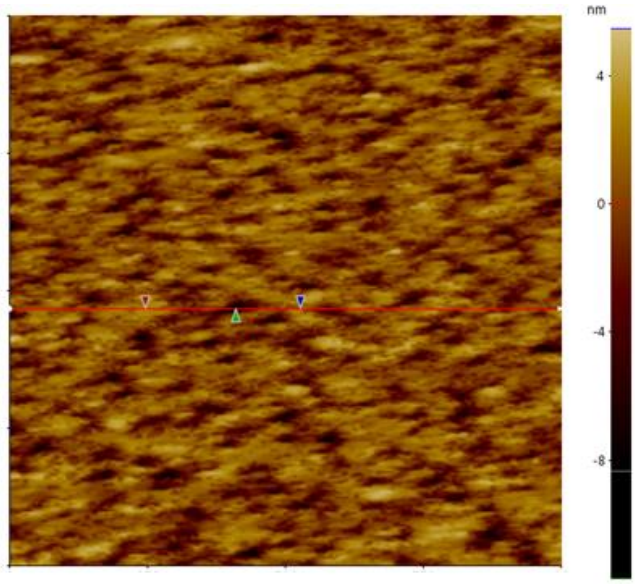

Figure 1.6 AFM scan image of 2 nm GaAs buffer/GaAs (111)A. The scan area is 1μm×1μm and the height difference (red and green) is 5.4 nm. Root-mean-square (RMS) roughness is 2.1 nm.

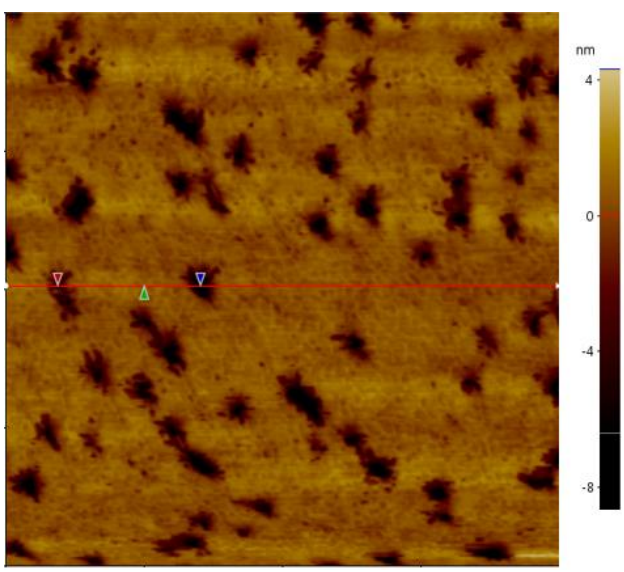

Figure 1.7 AFM scan image of 10 nm GaAs buffer/GaAs (111)A. The scan area is 1μm×1μm and the height difference (red and green) is 4.7 nm. Root-mean-square (RMS) roughness is 1.5 nm.

1.4. Motivation of the research

Nanostructuring is a primary strategy for increasing the TE figure of merit. When the surface-to-volume ratio increases, phonon boundary scattering effectively reduces the lattice's thermal conductivity, rather than the electrical conductivity. In particular, when the size of the TE material becomes similar to the mean free path (mfp) of photons, which is much larger than the mfp of electrons, the thermal conductivity can be significantly reduced. MBE growth technique controls atomic level growth and various growth conditions determine the TE figure of merit. Accurate control of the variables (size, doping, and defect) is essential for determining the relationship between one factor and the figure of merit. Hence, MBE is an appropriate growth technique for studying the TE effect. The RHEED oscillation and accurate control over the Bi flux facilitate easy control over the thickness of the grown film. An increase in the ZT has been reported for Bi_2Se_3 nanoribbons and nanowires. However, studies of Bi_2Se_3 nano-films are rarer than those on nanowires because the induced heat from the film is easily conducted to the contacting substrate. For thermal conductivity measurements using 3ω method, the TE material must be mechanically separated from the substrate. However, it requires the nanoelectromechanical systems (NEMS) technique because Bi_2Se_3 is soft, easily bendable, and thus, unstable when suspended. Hence, this report focuses on suspending the Bi_2Se_3 film and measuring the thermal conductivity.

TE studies by introducing doping or allow can also enhance TE performance

by increasing the power factor or decreasing the thermal conductivity. Effusion cells are filled with Ga and As for growing GaAs buffer layer, Bi and Se for Bi_2Se_3, and Sb, Te for doping. The following up study will cover the Te or Sb doping to the optimized Bi_2Se_3 growth process. Moreover, growth technique that is far different from the optimized condition results in surface defects. Surface defects usually result from the rapid growth rate and/or rough GaAs surface (without GaAs buffer layer). The step-by-step studies from thickness variation to doping or defect variations will utilize the physical comprehension how the physical quantities affect on the TE performance.

Chapter 2. Theoretical backgrounds

In this chapter, we will discuss the theoretical background of TE effects and why it is difficult to improve TE performance. Furthermore, we will discuss the method for measuring the thermal conductivity of MBE-grown Bi_2Se_3 film. The self-heating 3ω method with the nanomachining technique facilitates accurate measurements of thermal conductivity.

2.1. Thermoelectric effect

2.1.1 Seebeck effect

Thomas Johann Seebeck discovered the generated voltage from temperature difference. This phenomenon is called the Seebeck effect in which a temperature difference between two electric conductors or semiconductors produces

a voltage difference. The Seebeck voltages are usually very small which order of a few microvolts. However, some materials can generate up to a few millivolts. Bi_2Se_3, one of a representative of TE material, can generate around 100 microvolt when the temperature difference between cold junction and hot junction is 1 K at room temperature. The Seebeck coefficient is defined as the ratio between the generated voltage and the temperature difference. The Seebeck effect is an example of electromotive force, and the relevant equations for this are as follows:

$$E_{emf} = -S\Delta T \tag{2.1.1}$$

$$J = \sigma\left(-\Delta V + E_{emf}\right), \tag{2.1.1}$$

where S is the Seebeck coefficient, ΔT is the temperature difference between hot and cold junctions and J is the local current density. As in Figure 2.1, the charge carriers from hot junction move to the cold junction. For n-type materials, the charge carrier is electron and the voltage of hot junction will be higher than cold junction that is the sign of Seebeck coefficient is negative. By the way, for p-type materials, the charge carrier is hole and the voltage of cold junction is higher than hot junction, that is the sign of Seebeck coefficient is positive.

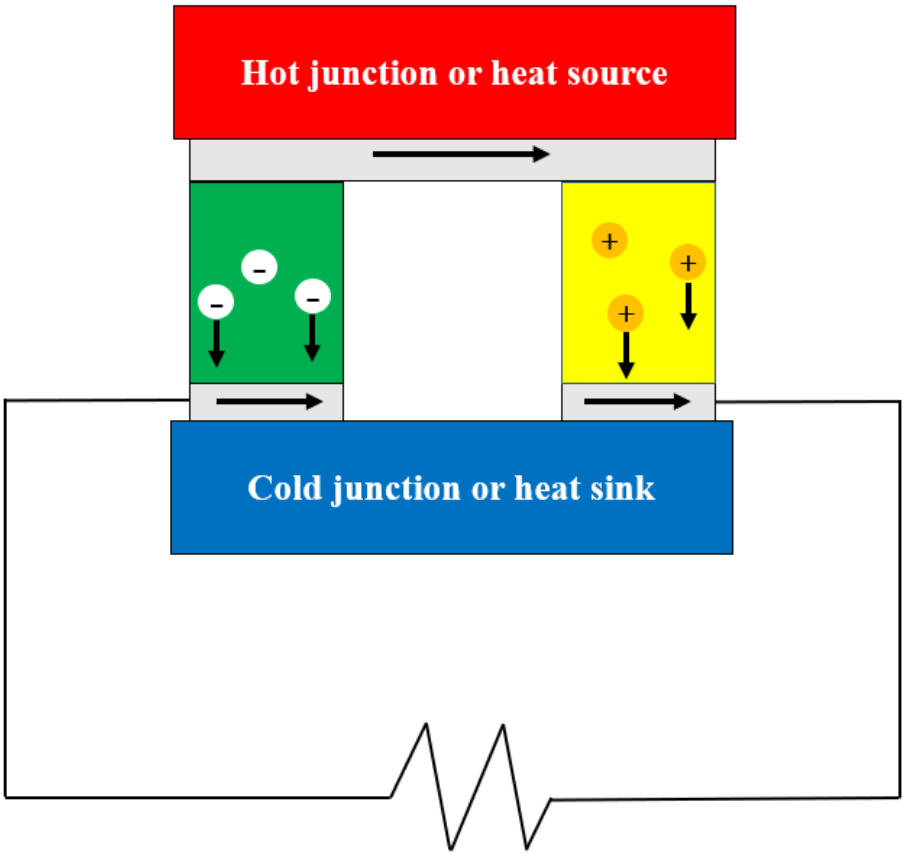

Figure 2.1 A thermoelectric circuit demonstrating the Seebeck effect.

2.1.2 Peltier effect

French physicist Jean Charles Athanase Peltier discovered the phenomenon which heating or cooling at a junction of two different conductors that have different voltages. When a DC current is sourced through a junction between two conductors, heat can be added or removed. This heat generated at the junction per unit time is expressed as:

$$Q = (\Pi_A + \Pi_B)I, \tag{2.1.3}$$

where A and B signify the two ends of the conductors, Π_A and Π_B are the Peltier coefficients of A and B, and I is the electrical current. The total heat generated by the current includes Joule heating and thermal-gradient effects. This effect can be thought as the back-action counterpart to the Seebeck effect. Consider a closed thermoelectric circuit. Then the Seebeck effect will drive a current, which in turn will transfer heat from the hot junction to the cold junction. Here, the Peltier coefficient is related to the Seebeck coefficient as:

$$\Pi = T\,S. \tag{2.1.4}$$

2.1.3 Thomson effect

The Seebeck effect assumes the temperature gradient and the Seebeck coefficient is not constant in temperature, hence a temperature gradient will result in a gradient in the Seebeck coefficient. If a current is sourced through this gradient, the Peltier effect will occur. That means the Seebeck effect and Peltier effect come from the sample physical origin. This is called the Thomson effect that is observed in 1851 by William Thomson. Thomson effect can be written as:

$$\dot{Q} = -\tau\,\vec{J}\cdot\nabla T, \tag{2.2.5}$$

where $\vec{J}$ is the current density, $\dot{Q}$ is the heat production rate per unit volume, and τ is the Thomson coefficient. The Thomson coefficient is related to the Seebeck coefficient as:

$$\tau = T\frac{dS}{dT}. \tag{2.2.6}$$

2.2. Thermoelectric figure of merit

The efficiency of TE devices is determined by the unitless figure of merit (*ZT*) defined as:

$$ZT = \frac{S^2\sigma T}{\kappa_l + \kappa_e} \tag{2.2.1}$$

where *S*, σ, *T*, κ_l, and κ_e denote the Seebeck coefficient, electrical conductivity, absolute temperature, lattice contribution to the thermal conductivity, and electrical contribution to the thermal conductivity, respectively. The maximum efficiency of a TE device is then described in terms of ZT where the maximum efficiency is given by

$$\eta_{max} = \frac{T_H - T_C}{T_H}\frac{\sqrt{1+Z\bar{T}} - 1}{\sqrt{1+Z\bar{T}} + T_C/T_H}, \tag{2.2.2}$$

where T_H is the temperature at the hot junction, T_C is the temperature at the cold junction, and $\bar{T}$ is the average of T_H and T_C. Good TE materials must possess a high Seebeck coefficient, high electrical conductivity, and low thermal conductivity. However, the correlations between *S*, σ, κ_l, and κ_e make the optimization of *ZT* difficult. In an n-type semiconductor, the negative electric charge does not only determine the electrical conductivity (σ), but they also contribute to the thermal conductivity (κ_e). According to the Wiedemann-Franz law, this correlation is expressed as:

$$\frac{\sigma T}{\kappa_e} = L, \tag{2.2.3}$$

where L is the Lorentz number. Hence, the figure of merit can be expressed as:

$$ZT = \frac{S^2/L}{1 + \kappa_l/\kappa_e} . \tag{2.2.4}$$

High ZT requires high electrical conductivity but also low thermal conductivity, and the Wiedemann-Franz law illustrates how the intrinsic properties of materials are in conflict for achieving a high TE figure of merit.

The correlations are not limited to the Wiedemann-Franz law. The Seebeck coefficient and electrical conductivity are also strongly correlated. A high Seebeck coefficient requires a single type of carrier because mixed n-type and p-type charge carriers will cancel out the induced Seebeck voltages. For metals or degenerate semiconductors like Bi_2Se_3, the Seebeck coefficient is given by:

$$S = \frac{8\pi^2 k_B^2}{3eh^2} m^* T \left(\frac{\pi}{3n}\right)^{2/3} , \tag{2.2.5}$$

where n is the carrier concentration and m^* is the effective mass of the carrier. Semiconductors with low carrier concentration possess a large Seebeck coefficient; see equation (2.2.5). However, low carrier concentrations will lead to low electrical conductivity; see equation (2.2.6):

$$\sigma = ne\mu , \tag{2.2.6}$$

where μ is the carrier mobility. Hence, for the degenerate semiconductors the power factor ($S^2\sigma$) will depend on the carrier concentration with a power of 1/3. The figure of merit usually peaks at carrier concentrations between 10^{19} and 10^{21} per cm^3, i.e., heavily doped semiconductors.

Moreover, a large effective mass of the charge carrier will result in a high Seebeck coefficient, but low electrical conductivity. Heavy carriers are associated

with low velocity, i.e., low carrier mobility. Hence, according to equation (2.3.5), the electrical conductivity will be low. In conclusion, the independent optimization of the thermoelectrical quantities, S, σ, T and κ_e, is considered impossible. The only independent component is the lattice contribution to the thermal conductivity (κ_l). There are several strategies to overcome these correlation and achieve high ZT. Doping, alloying, heterostructure, defect, nanostructuring, and the application of grain size and strain are used to enhance the ZT. Doping and alloying are used to optimize the carrier concentration, thus maximize the power factor. Other techniques are usually aiming to minimize the lattice contribution to the thermal conductivity.

2.3. Thermal conductivity

2.3.1 Steady-state methods

Thermal conductivity is the physical property of a material that measures of its ability to conduct heat. Thermal conductivity measurement gives fundamental understanding of the transport properties of carriers (electrons and phonons). The defining equation for thermal conductivity is given by the Fourier Law of heat conduction,

$$\boldsymbol{q} = -\kappa \nabla T, \tag{2.3.1}$$

where $\boldsymbol{q}$ is the heat flux, κ is the thermal conductivity, and ∇T is the gradient of the temperature. Dynamic methods that measure the thermal conductivity of a

material require to solve the time-dependent heat conduction equation. In experiment, dynamic methods measure thermal diffusivity and the thermal conductivity is then calculated. This indirect determination of the thermal conductivity brings additional uncertainties. But steady-state methods directly measure thermal conductivity based on the equation (2.3.1). Steady-state methods require planar, cylindrical, or spherical isotherms and measure heat flow through the sample directly or mount a reference material with known and similar thermal conductivity in series with the sample [36-38]. Major sources of effort in steady-state measurements include parasitic heat losses, especially for samples with small thermal conductance values. Hence, an accurate heat flow measurement is essential to minimize this error.

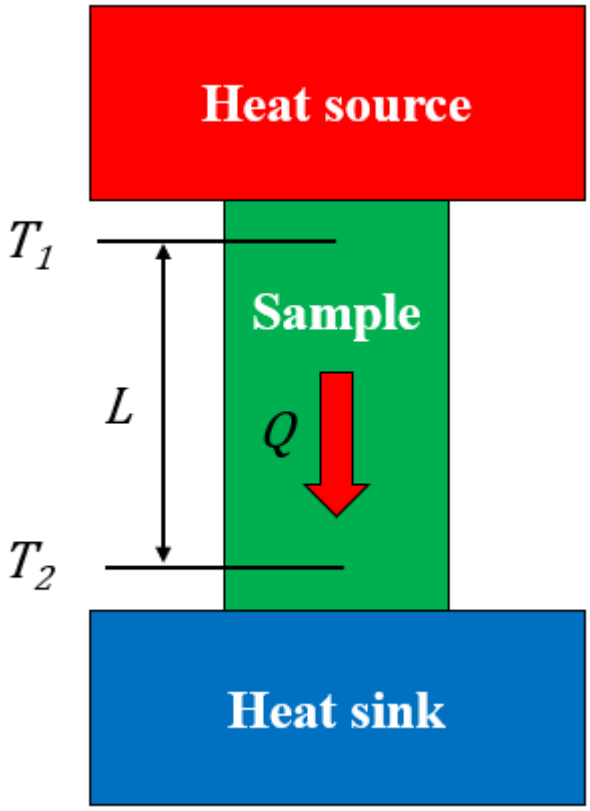

Figure 2.2 Schematic of steady-state methods commonly used for measuring the thermal conductivity of bulk materials. The thermal conductivity of the sample is directly measured

with the accurate values of T_1, T_2, Q, and geometrical factors.

2.3.2 Time-domain methods

Along with the development of the quantum mechanics, thermal properties of nanoscale sample are becoming more important than bulk. As the thickness of a thin film becomes comparable (or smaller) values of the mean free paths of phonons or electrons, the thermal conductivity of the thin film is greatly different from bulk counterpart due to the geometric constraints. Over the past a few decades, time-domain thermoreflectance (TDTR) has evolved as a reliable method to measure the thermal properties of a various types of materials including bulk and thin films with a thickness up to around 20 nm [39, 40]. The idea of TDTR is that once a material is heated, the change in the reflectance of the surface is dependent on its thermal properties. From the time dependent reflectivity measurement, thermal properties can be obtained from the corresponding model.

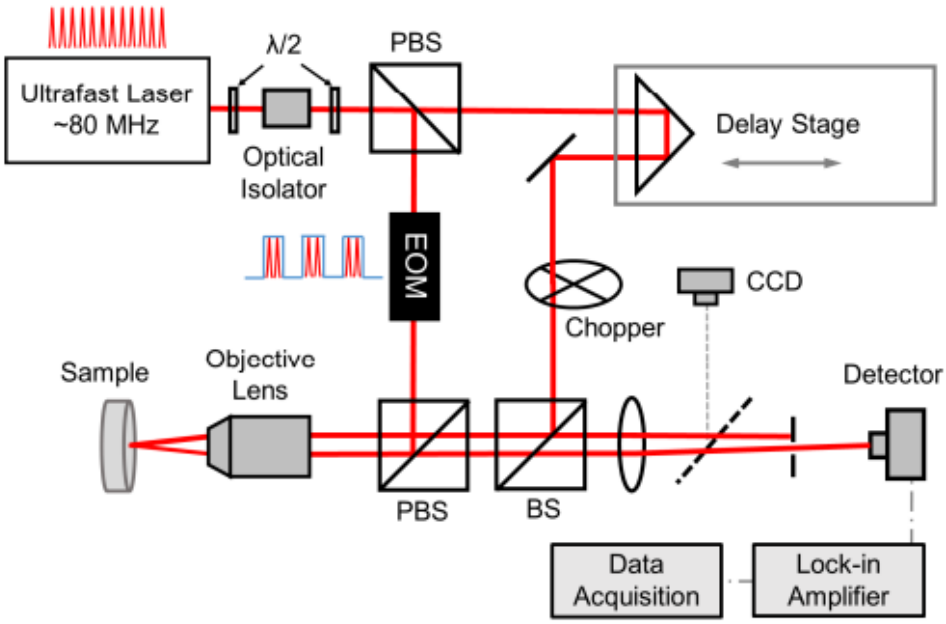

Figure 2.3 Schematic of a typical TDTR measurement setup. The PBS, BS, EOM, and λ/2 stand for polarizing beam splitter, beam splitter, electro-optic modulator, and half-wave plate, respectively [41].

2.3.3 Frequency-domain methods

In late 1980s, Cahill et al. introduced ideas of techniques for measuring the thermal conductivity [42]. Those methods are now called 3ω methods because AC current at frequency ω induces voltage signal at frequency 3ω, which directly related to the thermal conductivity of a material. 3ω methods can be used to measure the thermal conductivity of bulk, thin films that are suspended or supported. The cross-plane thermal conductivity of thin films can be measured by 3ω methods by heating deposited metal [Figure 2.4]. The film of interest is in contact with a substrate of high thermal conductivity. For accurate cross-plane measurements, low thermal conductivity films, long and wide heater line (metal) so that generated heat

can be approximated as 1D heat conduction. Also, thick enough substrate is essential for being approximated as semi-infinite, and avoiding high frequencies where the heat capacities of the film and heater matter (Eq. 2.4.9) [43].

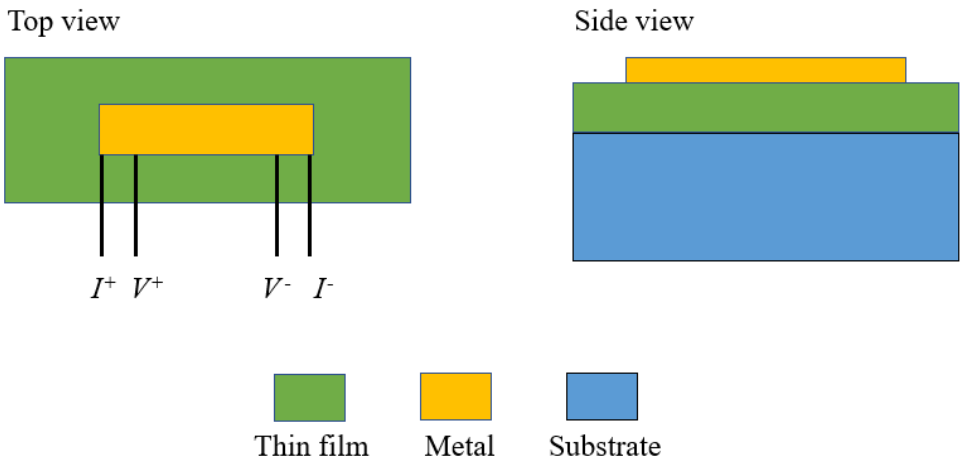

Figure 2.4 Measuring the cross-plane thermal conductivity of a non-metal thin film using 3ω methods.

For the case of supported film on a substrate, variable-linewidth 3ω method can be used. As in Figure 2.5, this method works well for thin films with a small cross-plane thermal conductivity conductivity because in-plane conduction will be dominant. The narrow heater regime can be defined as

$$\left(\frac{b}{d}\right)\left(\frac{k_z}{k_x}\right)^{\frac{1}{2}} \leq 0.1\,, \tag{2.4.1}$$

where b, d, k_x and k_z are half of width (Figure 2.6), thickness of the film, in-plane thermal conductivity and cross-plane thermal conductivity [44]. In the narrow heater regime, the resistance of heater is sensitive to both k_x and k_z. Hence, much greater width of heater is also necessary for determining k_z (Figure 2.5, left). In ideal case, in-plane heat conduction can be ignored so that, independent measurement of k_z is possible when the heater is wide enough.

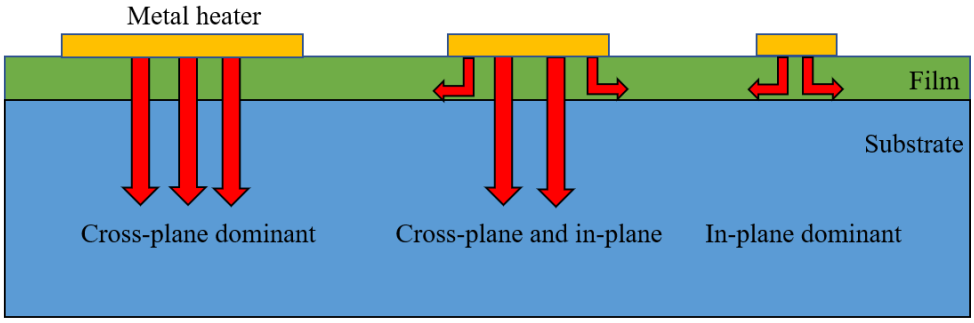

Figure 2.5 Schematic of the idea of variable-linewidth 3ω method. When the metal strip width is much larger than the thin film thickness (left), the heat conduction can be approximated to be vertical direction. As the width of metal heater gets shorter, heat conduction to the in-plane direction can't be ignored.

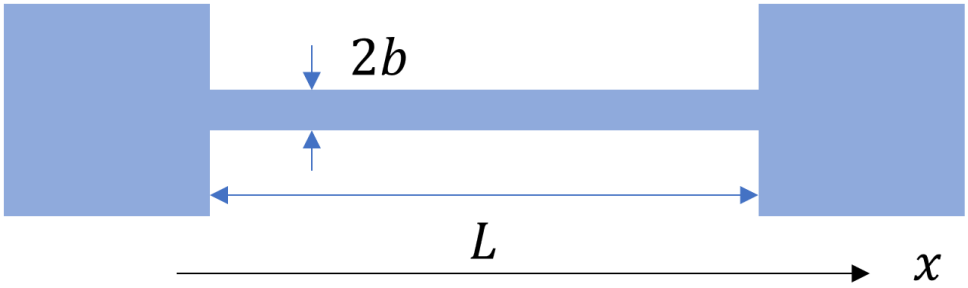

Figure 2.6 The schematic of the sample to measure the thermal conductivity with 3ω method.

Finally, for the case of suspended thin film, $3\boldsymbol{\omega}$ methods are straightforward. When the film of interest is electrically conducting with a stable $I-V$ curve, i.e. metal, metal film itself can be used as both electrical heater and temperature sensor. AC current with frequency $\boldsymbol{\omega}$ is passed through the suspended film to cause self-heating. This Joule heating results in temperature fluctuation with frequency $2\boldsymbol{\omega}$, and AC current ($\boldsymbol{\omega}$) passing through fluctuating resistor ($2\boldsymbol{\omega}$) will

induce 3$\boldsymbol{\omega}$ voltage (V=IR). This method is called self-heating 3$\boldsymbol{\omega}$ method, and it is used to measure the thermal conductivity of Bi_2Se_3, which shows metallic behavior due to Se-vacancies. When the film is not metallic, metal heater needs to be deposited on the film.

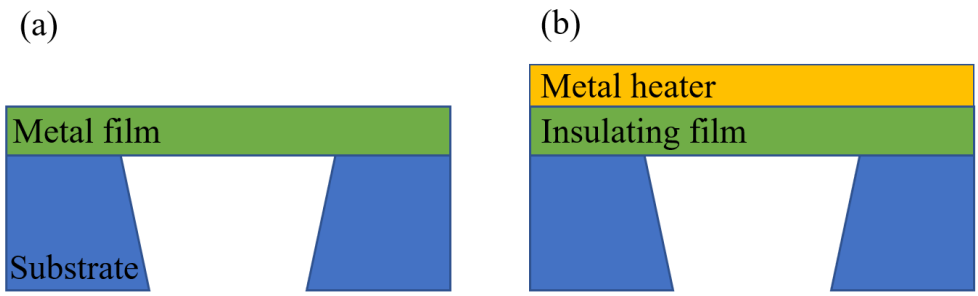

Figure 2.7 Side view of methods to measure the in-plane thermal conductivity of a suspended film of (a) metallic film and (b) insulating film.

2.3. Self-heating 3ω method

Consider a Bi_2Se_3 sample. An electrical current of the form $I_0 \sin\omega t$ is sourced from outside probes. This results in Joule heating of the form $0.5 I_0^2 R(1 - cos2\omega t)$, where R is the resistance of the metal. This periodic Joule heating results in temperature oscillation at a frequency of 2ω, which causes the resistance of the metal to oscillate at 2ω :

$$R_h(t) = R_0[1 + R'\Delta T_{DC} + R'|\Delta T_{AC}|cos(2\omega t)]\,. \qquad (2.4.1)$$

This leads to a voltage fluctuation at 3ω across the rod due to the injected electrical current at ω and the oscillation of the resistance at 2ω by the Ohm's law.

$$V_{3\omega}(t) = I_0 R_0 \left[\frac{1}{2} R'|\Delta T_{AC}| \cos(3\omega t)\right]. \qquad (2.4.2)$$

The amplitude of the voltage at 3ω is determined by the thermal properties because the $|\Delta T_{AC}|$ depends on the thermal conductivity and described by the 1D heat diffusion equation:

$$\rho C_p \frac{\partial}{\partial t} T(x,t) - \kappa \frac{\partial^2}{\partial x^2} T(x,t) = \frac{I_0^2 sin^2 \omega t}{LA} [R + R'(T(x,t) - T_0)], \quad (2.4.3)$$

with a proper initial condition (Eq 2.2.4) and boundary conditions (Eq 2.2.5, Eq 2.2.6):

$$T(x, -\infty) = T_0 \quad (2.4.4)$$

$$T(0,t) = T_0 \quad (2.4.5)$$

$$T(L,t) = T_0 \quad (2.4.6)$$

Consider a rod like model for the Bi_2Se_3 sample (Figure 2.1). The solution of Eq 2.3.3 can be written as:

$$T(x,t) - T_0 = \Delta_0 \sum_{n=1}^{\infty} \frac{[1-(-1)^n]}{2n^3} sin \frac{n\pi x}{L} \left[1 - \frac{\sin(2\omega t + \varphi_n)}{\sqrt{1 - cot^2 \varphi_n}}\right], \quad (2.4.7)$$

where $\Delta_0 = \frac{2I_0^2 R}{\pi \kappa A/L}$ and $cot\varphi_n = \frac{2\omega L^2}{n^2 \pi^2 \alpha}$. Then the resistance fluctuation can be expressed as the temperature fluctuation by assuming the R-T of the material is linear:

$$\Delta R = \frac{R'}{L} \int_0^L [T(x,t) - T_0] dx$$

$$= R' \Delta_0 \sum_{n=1}^{\infty} \frac{[1-(-1)^n]^2}{2\pi n^4} \left[1 - \frac{\sin(2\omega t + \varphi_n)}{\sqrt{1 - cot^2 \varphi_n}}\right], (2.4.8)$$

n=2 term is canceled, and the n=1 term can be expressed as:

$$V_{3\omega}(t) \approx \frac{2I_0^3 LRR'}{\pi^4 \kappa A \sqrt{1 + (2\omega\gamma)^2}} \sin(3\omega t - \theta), \quad (2.4.9)$$

where $\gamma = \frac{L^2 \rho C_p}{\pi^2 \kappa}$ is the thermal time constant.

In the low frequency limit ($\omega\gamma \sim 0$), the 3ω voltage can be expressed as:

$$V_{3\omega} \approx \frac{2I_0^3 LRR'}{\pi^4 \kappa A}, \tag{2.4.10}$$

or it can be expressed as

$$\kappa \approx \frac{2I_0^3 LRR'}{\pi^4 A V_{3\omega}}. \tag{2.4.11}$$

Hence, by measuring $V_{3\omega}$ and the temperature-resistance relation, one can determine the thermal conductivity of the material.

The theoretical validations of 3ω method are checked by the cubic relation between the current I and the voltage $V_{3\omega}$ (consider the Eq. 2.3.2 and Eq. 2.3.10) and the relation between the frequency f and the voltage $V_{3\omega}$ (Eq 2.3.9). This study conducts the current sweep for determining the thermal conductivity, but also obtain the validity of the 3ω method. Also, from the frequency sweep that is not presented in this dissertation, the voltage $V_{3\omega}$ does not change below 100Hz. The measurement is done at 13Hz, and this frequency is low enough to ignore the thermal time constant ($\omega\gamma \sim 0$).

Chapter 3. Sample preparation

Sample preparation

In this chapter, we will show the process of MBE growth of Bi_2Se_3 on the semi-insulating substrate GaAs (111)A. The fabrication process for realization of a freely suspended structure is done by selective wet etching followed by critical point drying. The suspended Bi_2Se_3 enables us to adopt the 3ω method.

3.1. MBE growth of Bi_2Se_3

3.1.1 Preparation

The epi-ready grade of semi-insulating GaAs (111)A substrate is attached to the molybdenum block (sample holder) by indium in a clean environment. The

block is then mounted into the moving cart that is loaded in the transfer chamber. After loading, the turbo pump maintains a vacuum in the load lock chamber (~10^{-5} torr). When the ion pump is turned on, the valve between the turbo pump and the chamber is closed. After a few hours, the pressure of load lock chamber becomes less than 10^{-7} torr. Then the gate valve between the load lock chamber and the prebaking chamber can be open and the cart is moved to the prebaking chamber. One of the molybdenum block is then mounted on the prebake heater and backed at 500°C (less than the desorption temperature) for 2 hours to remove contaminations on the substrate. The temperature of the heater is controlled by a temperature controller (set the PC value as 8.5~9.0). During the prebake process, the other samples with moving cart should be isolated from prebake chamber to prevent pollution by the prebake. After 2 hours, stop heating and wait until the sample cools down enough (below 200°C). When all the samples are prebaked, the cart with sample holders is moved to the transfer chamber and the sample holder is ready to be loaded on the main chamber.

The main chamber of MBE system is cooled down by LN2 for 6 hours before loading the sample. Then the pressure of the main chamber is maintained around 10^{-9} torr which is a necessary condition for high quality of growth. Effusion cells are charged with Bi (99.9999%), Se (99.999+%), Ga (99.999%), and As (99.99999+%). The temperature controllers accurately control the temperature of effusion cells, and the corresponding flux is measured by the gauge as follows. First, Set the temperature of Ga cell as 785°C (2.2×10^{-8} Torr) and Bi cell as 570°C (1.0×10^{-7} Torr). Second, Set the temperature of As cell as 290°C (5.0×10^{-7} Torr) and Se cell as 164°C (7.0×10^{-7} Torr). Here, the flux of As and Se are relatively high than Ga and Bi. Thus, make sure that the flux of Ga and Bi are measured by ion gauge

before setting the temperature of As and Se cell. When the temperatures of As and Se cells are 290°C and 164°C, respectively, the pressure of the chamber becomes 1.0×10^{-7} Torr, hence accurate flux measurements of Ga and Bi are not possible (less significant figures). Also, be careful when control the temperature of As and Se cells because if the PID values are not optimized, the cell temperatures can be higher than the target values. These temperatures are determined to keep the flux ratio of Ga : As = 1 : x (20>x>16) and Bi : Se = 1 : y (20>y>16) to prevent the As vacancy of GaAs and Se vacancy of Bi_2Se_3. Also, the relation between the temperature of the cell and the flux is measured every 2K (Se, As) or 5K (Ga, Bi).

3.1.2 Growth process

After loading the sample holder into the main chamber, the desorption is done at a substrate temperature of 700°C for 10 minutes in the As-rich condition for preventing As-vacancy. Before the desorption starts (around 500°C), open the As effusion cell so that prevent As-vacancy. After the reflection high-energy electron diffraction (RHEED) pattern of GaAs substrate appears, we slightly lower substrate temperature to 680°C. Then 40 nm GaAs buffer layer is grown at a deposition rate of 1 nm/min under the As/Ga flux ratio of ~ 20. During the growth of GaAs layer, RHEED pattern becomes streaky and the growth rate is measured from RHEED oscillation. Then, Ga shutter is closed and the temperature of sample holder is cooled down to 300°C. Below 450 °C, the chamber environment is changed to Se-rich condition (close the As shutter and open the Se shutter) when growing Bi_2Se_3 layer.

Then, 200 nm Bi_2Se_3 epifilms were grown at a substrate temperature of 350˚C with a growth rate of 2nm/min under Se-rich conditions with the flux ratio (Φ_{Se}/ Φ_{Bi}) of ~ 20. At first a few layers of Bi_2Se_3, the RHEED pattern becomes unclear. Then the RHEED pattern becomes bright and streaky after 4 quintuple layers (QL) are grown. After the growth, the sample is cooled down up to 100˚C while the Se source is open to prevent Se vacancies. Below 150˚C, the RHEED pattern is getting unclear due to the amorphous Se-capping layer.

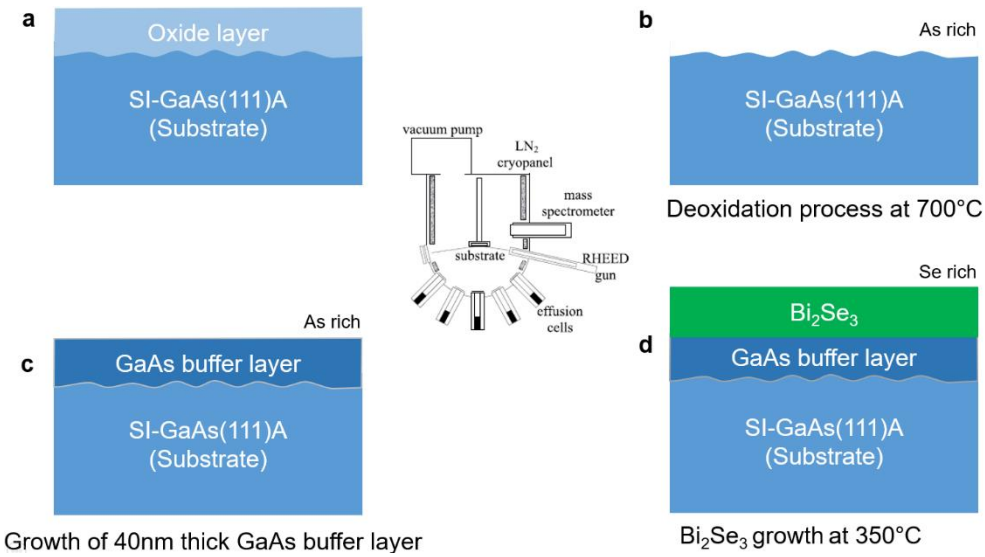

Figure 3.1 The schematic of the growth process.

3.1.3 Analyzation

From in-situ RHEED monitoring during the growth as well as post-growth morphologies characterized by non-contact mode AFM and high-resolution XRD, the resulting film shows similar to the Bi_2Se_3 that reported elsewhere. XRD reveals the grown Bi_2Se_3 is highly c-axis oriented, and AFM scan image shows the trigonometric spiral shaped Bi_2Se_3.

MBE growth process:

1. Epi-ready GaAs (111)A is indium-bonded on the Mo-block at a hotplate.
2. Mo-block is loaded on the moving cart.
3. Vent the loading chamber and load the cart.
4. Evacuate by turbo pump backed up by rotary. At high vacuum, turn on the ion pump (turn off the turbo).
5. Open the gate valve, and move the cart to prebake chamber. The Mo-block is transferred to the heater. The GaAs substrate is baked at 500 °C for 2 h.
6. Set the proper temperatures of effusion cells. First, Ga cell as 785°C (2.2×10^{-8} Torr) and Bi cell as 570°C (1.0×10^{-7} Torr). Later, As cell as 290°C (5.0×10^{-7} Torr) and Se cell as 164°C (7.0×10^{-7} Torr)
7. Open the gate valve and move the cart to transfer chamber. Close the gate valve between prebake and transfer chambers. Open the gate valve of the main chamber.
8. Transfer and load the Mo-block to the main chamber. Close the gate valve. Set the proper substrate temperature (680 °C) for desorption. Open the As-shutter to prevent As-vacancies.
9. Bake the substrate at 680 °C until the RHEED pattern of GaAs appears (usually takes time around 30 minutes). Raise the substrate temperature up to 700 °C.
10. Open the Ga-shutter, then the growth starts. Growth GaAs buffer layer with thickness 40 nm (40 minutes).
11. Close the Ga-shutter to stop the growth. Set the substrate temperature as 300 °C. At around 400 °C, close the As-shutter because As-vacancy does not occur at this temperature.
12. Open the Se-shutter, then the chamber becomes Se-rich condition. Open the

Bi-shutter to start the growth.

13. Close Bi-shutter and set the substrate temperature at 100 °C. Near 100 °C, the RHEED pattern disappear meaning that the amorphous Se-capping layer is deposited.
14. Analyze the grown films with AFM, high-resolution XRD and SEM.

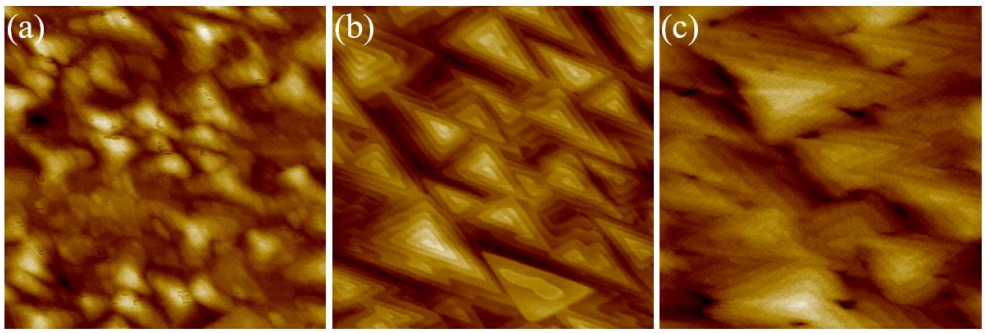

Figure 3.2 1μm×1μm AFM scan images of Bi_2Se_3. grown at the temperature (a) 200 °C (b) 300 °C (c) 400 °C.

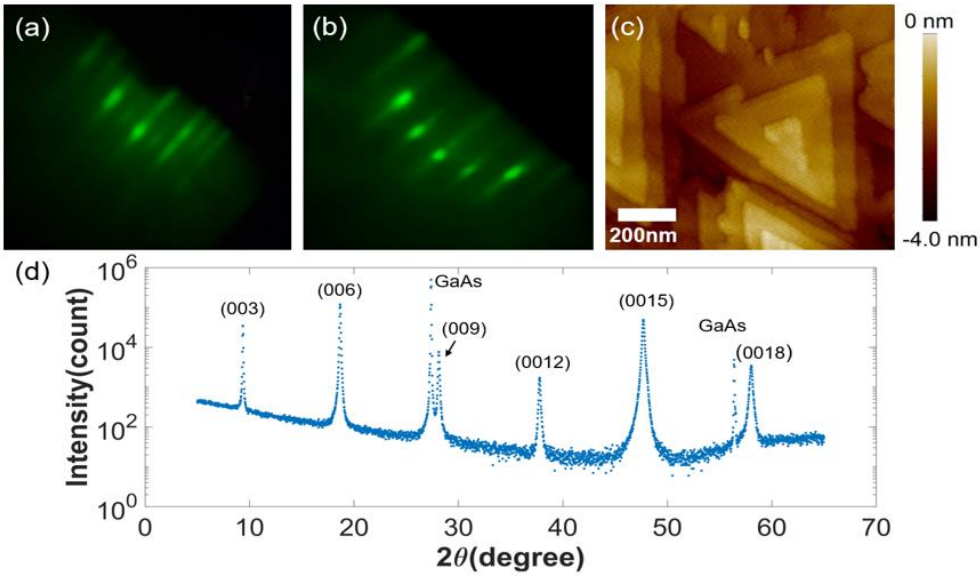

Figure 3.3 RHEED patterns during epitaxial growth of (a) the GaAs buffer layer (40 nm) and (b) Bi_2Se_3 (300 °C), (c) 1μm×1μm AFM scan image, (d) high-resolution X-ray

diffraction of Bi_2Se_3.

3.2. Sample fabrication

3.2.1 Patterning

Commercially available SEM (TESCAN, VEGA TS 5130MM) that is controlled by nano patterning generate system (NPGS) is used for pattering the sample. The accelerating voltage is kept as 30 kV for high contrast and the working distance is set to 3.0 mm for accurate pattering. The electrometer (Keithley Instruments, 617 programmable electrometer) is used for measuring the current when the electron beam is focused to the Faraday cup made of cupper. For the positive e-beam lithography, we coat E-beam resist (PMMA 950K-A4) using a spin coater (4000rpm, 60sec) followed by a bake process (180°C, 120sec). With the proper dose of electron beam, we can achieve 20nm line width pattern. For a low temperature (5°C) develop for a high contrast, the value of area dose is set to 330 $\mu C/cm^2$. Then a 3:10 solution of distilled water and isopropyl alcohol (IPA) is used for developer. The sample is developed in this solution for 2 minutes at 5°C (longer time to prevent under develop). Then the sample is rinsed by IPA for 10 seconds followed by blown dry by a nitrogen gas. For the inverse lithography, the photo-resist (AZ5206) is coated using a spin coater (4000rpm, 60sec) followed by a prebake process (90°C, 90sec). We use the area dose as 100 $\mu C/cm^2$ which is the optimized value for high contrast. Then the UV bare exposure is done by a mask aligner (MIDAS, MDA-400S) for 40 sec with

the intensity of 25mW/cm^2. Then the sample is baked again at 120°C for 3 min. Then, the sample is developed by MIF 300 at 5°C for 120 sec. Finally, the sample is rinsed by distilled water for 10 sec and blown dry by N2 gun. Here, we find that the time of post-bake (3 min) and the low temperature develop (5°C) are essential for achieving a good adhesion between Bi_2Se_3 and photo resist.

The positive patterning process is:

1. PMMA 950k A5 is spin-coated at 4000 rpm for 1 min
2. Baked at a temperature 180 °C for 2 min.
3. Loaded in the SEM sample holder.
4. Electron beam writing with an area dose of 330 μC/cm^2.
5. Developed by 3:10 solution of distilled-water and IPA for 2 min at 5 °C.
6. Rinsed with IPF for 10 sec and dried by N2 gun.

The image reversal patterning process is:

1. The resist, AZ 5206 is coated at 4000 rpm for 1min.
2. Baked at a temperature 90 °C for 90s (prebake).
3. Electron beam writing with an area dose of 60 μC/cm^2.
4. Flood UV exposure using mask aligner for 40 s.
5. Baked at 120 °C for 3 min.
6. Developed in the MIF 300 for 2 min at 5°C.
7. Rinsed by distilled-water for 20s.
8. Blown by N2 gas.

(Here, one can use higher e-beam dose like 100 μC/cm^2 to achieve higher contrast, but then it needs longer develop time (3 min))

3.2.2 Metallization

The adhesion between Bi_2Se_3 and Gold deposited by e-beam evaporation is very poor even when the adhesion layer (Ti) is deposited. Hence, DC sputtered platinum is used for electrodes (pad, leads), temperature sensors, heaters, and voltage probes. DC sputter results in much better adhesion than the e-beam evaporator without additional adhesion material. The sputter system consists with four sputtering guns (AJA International, A320) with four sources (Pt, Py, Al, Cu). Also, the system consists with the load-lock chamber, main chamber, two turbo pumps, and one ion pump. The base pressure of the main chamber is kept around 2×10^{-8} Torr by an ion pump (VMT Kleenion pump, VIP 120). The base pressure of the load-lock chamber is kept 2×10^{-5} Torr.

The sputter deposition procedures are following:

1. Attach the samples on the sample holder with kapton tape that is resistive with high temperature.
2. Vent the load-lock chamber. Open all the three valves between the N2 cylinder and the load-lock chamber.
3. Mount the sample holders in the load lock chamber. Close the N2 valves. Then turn on the turbo pump (Pfeiffer Vacuum, HiCube) for achieving high vacuum in the load-lock chamber.
4. Open the valve for cooling water. Turn on the rotary pump (WOOSUNG VACUUM, MVP90) for backing the main turbo pump. Make sure that the gate valve between the main turbo pump and the main chamber is closed.

5. After at least 10 min, turn on the main turbo pump. When the main turbo is fully running (42,000 RPM), turn off the ion pump. Open the gate valve between the turbo and the main chamber (We use ion pump normally but during the deposition, we use turbo pump.).
6. Check the vacuum gauge (VARIAN, XGS-600). When the pressure of the load-lock chamber is below 2×10^{-6} Torr, open the gate valve between the load-lock chamber and the main chamber right after closing the valve for the turbo pump (Pfeiffer Vacuum, HiCube) to prevent reflux.
7. Load the sample holder to the main chamber. Make sure that all the three pins are locked. Close the gate valve between the load-lock chamber and the main chamber. Open the valve between the load-lock chamber and the turbo pump.
8. The deposition is ready. Adjust the height of the sample properly. Open the Ar cylinder and control the Ar flow (20 sccm) through a flow controller (ATOVAC, GMC1200). Turn on the power supply (Advanced Energy, MDX 500) and set the output power as 30 W.
9. The deposition starts when the shutter is open. The thickness of Pt is measured by thickness monitor (INFICON, SQM-160). After finish the sputtering, follow the steps backward.

3.3.3 Suspended structure

The self-heating 3ω method demands suspended structure to minimize the heat diffusion to the substrate. A 1:6 (volumetric) solution of citric acid (citric acid 1kg melted in water 2L) and H_2O_2 is used as the etchant for the GaAs substrate. To minimize the chemical reaction between the etchant and the Bi_2Se_3, the etch windows are patterned using the PMMA and SEM. The windows are apart from Bi_2Se_3 pattern by 1μm.

Then, the etching process are:

1. HCl treatment for 10 s to remove oxide residue.
2. DI wash for 1 min.
3. Etching for 10 min in the citric acid solution (etch rate is around 150nm/min).
4. DI wash for 1 min.
5. Put the sample in the acetone to remove PMMA residue.
6. Put the sample in the IPA.
7. Critical point drying (Tousimis, autosamdri-815)

The surface tension of IPA can result the collapse of suspended Bi_2Se_3 structure. The critical point dryer (CPD) is used to dry samples that have had a final rinse in IPA. CPD make use of liquid CO2 under high pressure and low temperatures to remove the liquid residue by avoiding the phase transition boundary from liquid to gas. The automatic process consists with cool, fill, purge, heat, bleed and vent. This MEMS technique enables to suspend 20 nm thick Bi_2Se_3. The suspended sample is then

loaded onto the SEM. The length and width are then measured by the SEM measurement tool. From the tilted view, we make sure that the Bi_2Se_3 is suspended. Bi_2Se_3 is flexible, hence sometimes it contacts the GaAs substrate.

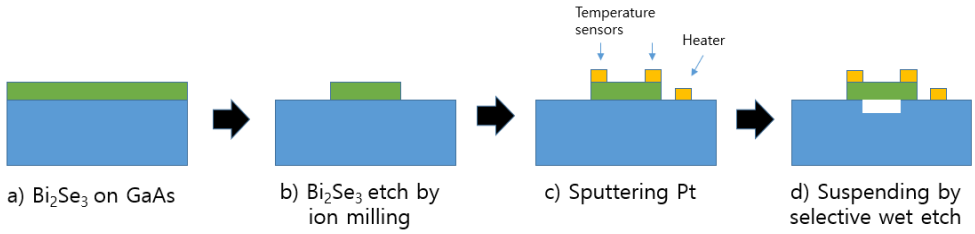

Figure 3.4 The simplified schematic of the fabrication from the film to suspended structure.

Chapter 4 Measurement and Analysis

In this chapter, we will describe the measurement method of the thermoelectric figure of merit. The suspended Bi_2Se_3 sample is vulnerable to the vibration of the cryostat, hence a quick and simultaneous measurement is needed. Also, the calculation of the Seebeck coefficient from the measurements of the Pt resistances and voltage different and the thermal conductivity from the measurements of the Pt resistance and 3ω voltage.

4.1 Measurement setup

The sample is bonded onto a PCB (printed circuit board) chip carrier by GE varnish to insure firm adhesion. This PCB is fixed on a copper block (sample holder, 2cm × 2cm × 2cm) with a heater (20 Ohm). The contact pads of PCB are bonded to

the sample pads by Au wire using wedge-type wire bonder (Kulicke&sofa, K4523). We use 8 pads for the two Pt temperature sensors to measure the resistance by 4 probes method and to measure the voltage difference, and 2 pads for a Pt heater that is used to make the temperature gradient. Then the sample is loaded on the cryostat that can maintain up to 20-400K. The cryostat consists with a compressor filled with He, cold head and vacuum chamber. The temperature controller and measurement instruments are connected to feedthrough of the cryostat. The cryostat chamber is pumped by a turbo pump backed up by a rotary pump with the base pressure of about 10^{-4} Torr.

To measure the Seebeck coefficient, two DSP lock-in amplifiers (Stanford Research Systems, SRS 830), a DC source (Keithley, 2400), and a multimeter (Keithley, 2700 multimeter/Data Acquisition system) are used. Two lock-in amplifiers are set at the frequencies 27 Hz, 37 Hz, respectively. One is to measure the hot side Pt resistance and the other one is to measure the cold side at the same time. To minimize the Joule's heat from Pt thermometer, small current (5 μA) is used by using the voltage divider (5 V output with 1 MΩ load resistor). The DC source (2400) is used to make temperature gradient by flowing current (30 mA, 0.2 W) on the Pt heater (300Ω at room temperature). The multimeter (2700) is used to measure the voltage difference between two sides of the Bi_2Se_3.

To measure the thermal and electrical conductivities, two DSP lock-in amplifiers are used. The one lock-in amplifier is locked by the other one, hence they measure the 1ω (electrical) and 3ω (thermal) signals simultaneously. Similarly, the voltage is converted to the current by using voltage divider to simplify the measurement setup. The compressor and temperature controller (Lakeshore, LS330) are used to sweep the temperature (20-400K). The electronics are set to remote mode

and connected to a PC by GPIB-to-USB cables and automatically controlled by "MATLAB" commands.

4.2 Measurement scheme

Figure 4.1 shows the SEM image of the sample. All the probes (blue) are sputtered platinum and the Bi_2Se_3 (red) are incorporated in the size of 1200 μm × 1200 μm (pads are not included in the figure). Two Pt thermometers are connected to two different lock-in amplifiers. A heater is connected to a DC source and voltage probes are connected to a multimeter. To calibrate the Pt resistances to the temperatures, the resistances of Pt thermometers are measured before turn on the heater (R1, R2). Then, the heater is turned on with a power of 0.2 W (current of 30 mA). With a proper time delay (10 s) to be thermal equilibrium, the resistances of Pt thermometers are measured (r1, r2) and the voltage difference between the Bi_2Se_3. Make sure the lock-in probes are disconnected when measuring the voltage because lock-in probes makes the two sides grounded. Hence, we use 12V relay switch operated by DC voltage source (YOKOGAWA, GS200) to disconnect/connect lock-in amplifiers. The GaAs temperature sensor is attached on the copper block (sample holder) and considering the high thermal conductivity of the copper, we can consider the sample temperature is the same as the copper. The resistance of GaAs sensor is converted to the temperature (T) by the temperature controller (LS330). Then, two linear plots (R1vsT and R2vsT) are used to calculate the temperature gradient (Figure 4.2).

$$R1 = \alpha_1 T + \beta_1, R2 = \alpha_2 T + \beta_2 \ , \tag{4.1}$$

where α_1, α_2 are the temperature coefficients of resistance, and β_1, β_2 are the resistances at 0 K (linear approximation). Then r1 is converted to temperate, T1, as

$$T1 = \frac{(r1 - \beta_1)}{\alpha_1}, \ T2 = \frac{(r2 - \beta_2)}{\alpha_2} \ . \tag{4.2}$$

With the voltage difference (ΔV=V1-V2) measured by the multimeter, we can calculate the Seebeck coefficient as

$$S = -\frac{\Delta V}{\Delta T} \ . \tag{4.3}$$

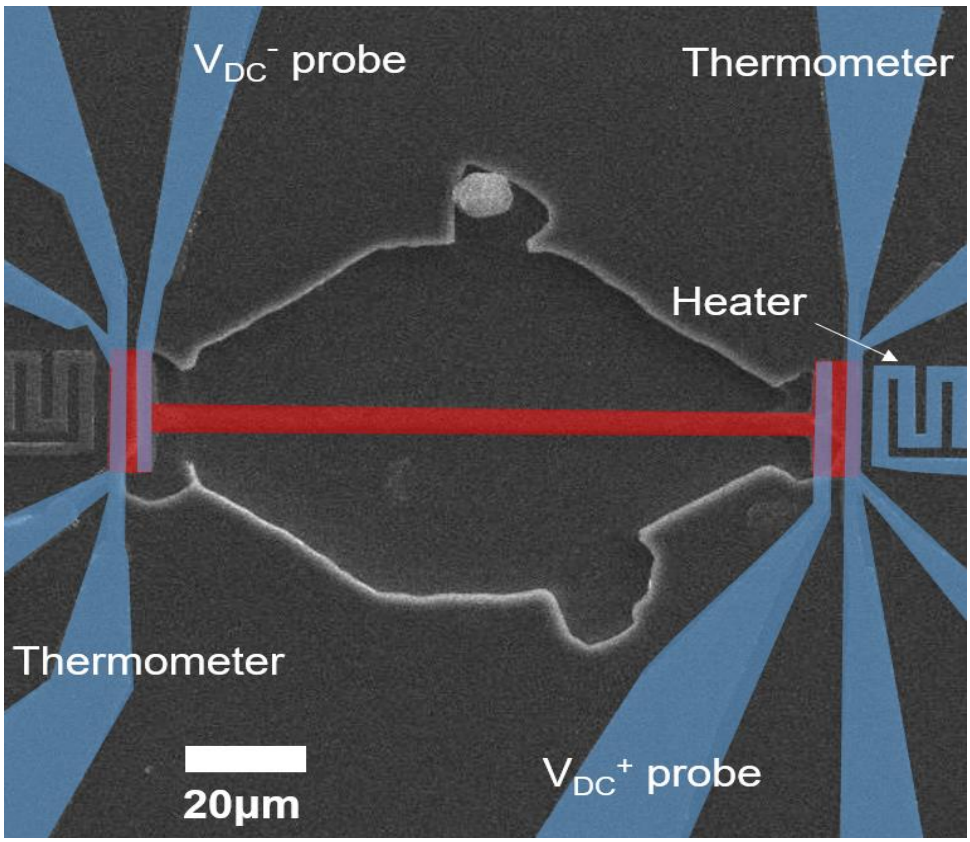

Figure 4.1 Schematic of Seebeck coefficient measurement. SEM image of the sample and the roles of the probes.

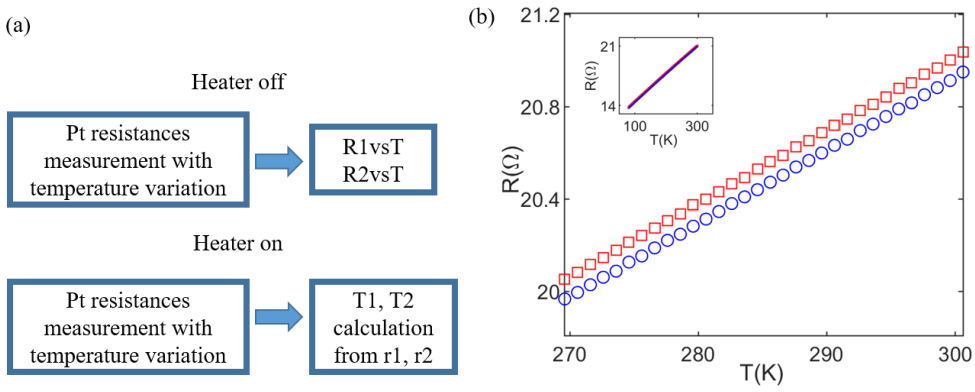

Figure 4.2 (a) The scheme of the measurement of the Seebeck coefficient. (b) Measurement data of R-T of two Pt thermometers.

Figure 4.3 illustrates the measurement scheme of thermal and electrical conductivity with the same sample. Two lock-in amplifiers (Figure 4.4) are connected to the sample, one is to measure the electrical conductivity (1ω), and the other one is to measure the thermal conductivity (3ω). To validate the 3ω method, the AC current sweep is needed at fixed frequency. The frequency 13 Hz is low enough to ignore the heat capacity term in the thermal conductivity. Similar to the Seebeck coefficient measurements, the sample temperature was varied from 20 K to 400 K. From these measurement, we recorded the electrical conductivity σ, $V_{3\omega}$, and determined $R' = [R(T_1) - R(T_2)]/[T_1 - T_2]$ so that we calculated the thermal conductivity as:

$$\kappa \approx \frac{4RR'LI^3}{\pi^4 A V_{3\omega}}, \tag{4.4}$$

where L is the length and A is the cross-sectional area. The 1ω measurement is the well-known 4-probe resistance measurement. From the resistance measurement (1ω) with the geometrical factors, the electrical conductivity is calculated as:

$$\sigma \approx \frac{L}{AR}. \tag{4.5}$$

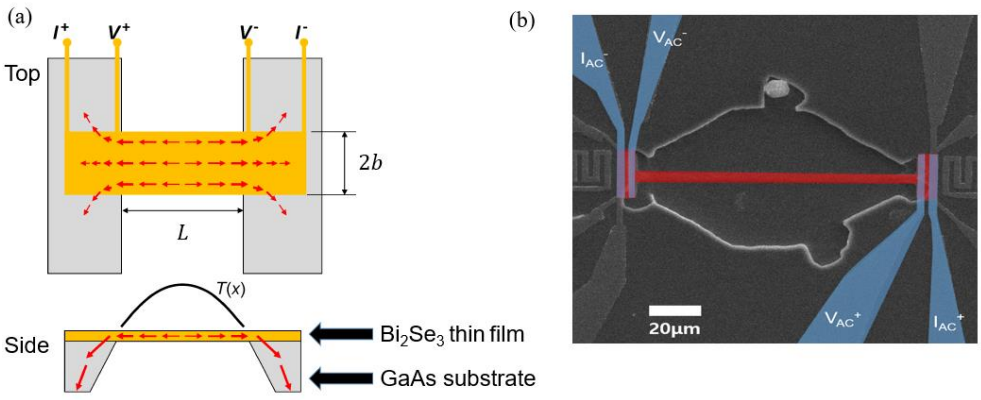

Figure 4.3 (a) The scheme of the 3ω device. (b) The SEM image of the sample. Blue colored Pt probes are connected to two lock-in amplifiers.

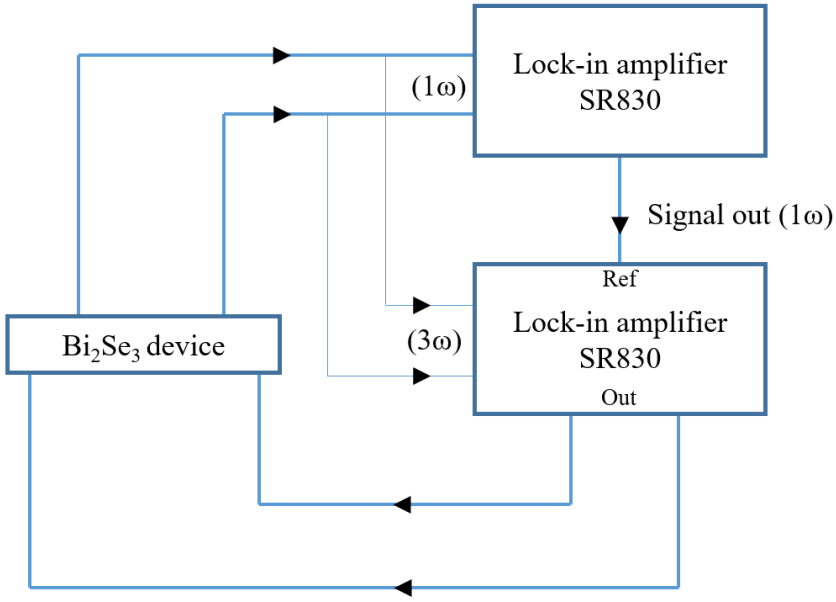

Figure 4.4 Instrumentation to measure the thermal conductivity and electrical conductivity simultaneously.

4.3 Thickness variation of Bi_2Se_3

The above processes are done by several different Bi_2Se_3. The one of the main factor determining the thermal conductivity, electrical conductivity, and Seebeck coefficient is thickness. Electrical and thermal conductivities become smaller when the material is become thinner. Especially, when the surface to volume ratio increases, the phonon scattering is much more increasing than the electron. Hence, it is known that the nanostructuring can enhance the thermoelectric figure of

merit by reducing the lattice thermal conductivity. Here, three different thick (150 nm, 200 nm, 300 nm) Bi_2Se_3 are fabricated to samples and measured with above method. The thickness is determined by the growth process, especially the growth time and the flux of Bi that determine the growth rate. The growth rate is measured by RHEED oscillation, then the thickness is measured by SEM side view and profilometer. Both measurements show similar values.

The measured thermal conductivity is shown in Fig. 4.5. All the three different Bi_2Se_3 shows that the thermal conductivities decrease when the temperature increases and the thickness decreases. The thermal conductivity of 300 nm thick Bi_2Se_3 is similar that of bulk Bi_2Se_3. By decreasing the thickness, the thermal conductivity is reduced by a factor of 3. The main errors of the measurement come from the measurement of the geometry and $\mathrm{R}' = [\mathrm{R}(T_2) - R(T_1)]/[T_2 - T_1]$. The thickness of grown Bi_2Se_3 is measured by SEM and profilometer. The measured value has an error of around 5%. In the determination of R', the temperature difference $T_2 - T_1$ is measured by the temperature controller (LS330). However, its resolution around the room temperature is 0.1K. The data shown in Fig.4.6 has a temperature step of 5K. Hence, around 4% of error occurs from the determination of R'. The remain main error occurs from the measurement of $V_{3\omega}$. When the thickness decreases, the suspended structure is getting unstable. The temperature of the chamber is decreasing by the He gas compression that causes the vibration of the chamber. This seems to cause the slight break of the thermal equilibrium. The thermal conductivity is calculated by the Eq 2.2.11. From the current sweep and $V_{3\omega}$, the value $I^3/V_{3\omega}$ is calculated from the slope of the linear plot of I^3 versus $V_{3\omega}$.

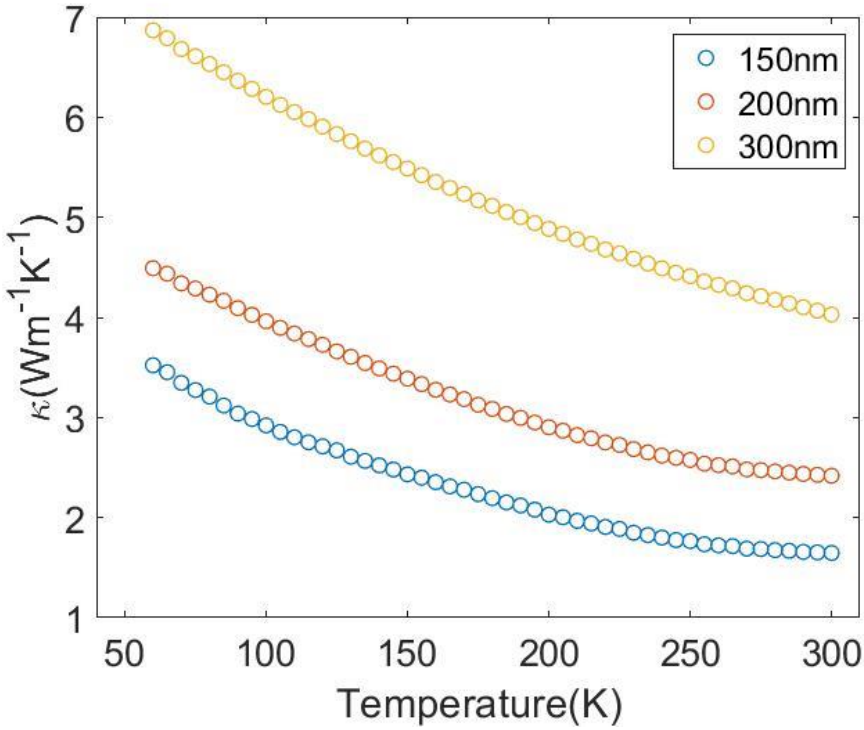

Figure 4.5 The thermal conductivity of Bi_2Se_3 with the temperature range of 60K – 300K.

When measuring the thermal conductivity, 1 ω measurement is done at the same time to determine R′ and the electrical conductivity. Its result is shown in Fig. 4.6 below. The resistance – electrical conductivity behavior shows metallic that implies Se-vacancies are highly concentrated. The Se-vacancies acts as an electron donors, hence the grown Bi_2Se_3 can be considered as a highly n-doped semiconductor.

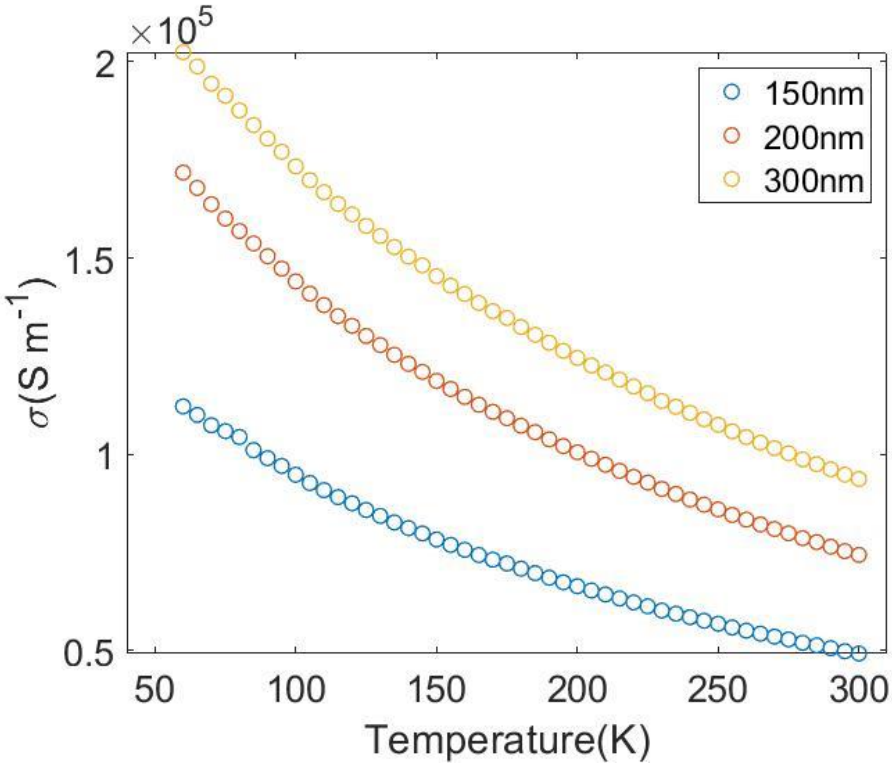

Figure 4.6 The electrical conductivity of Bi_2Se_3 with the temperature range of 60K – 300K.

The Seebeck coefficient of the Bi_2Se_3 is shown in Fig. 4.7. The Pt heater locates at both sides of the Bi_2Se_3 to exclude the anti-symmetry effect (artifacts). In this report the right one (Fig. 4.2) is used to make the temperature gradient. The 30mA DC current is driven to the heater. Then the resistances of the Pt thermometers that locate at both end side of the Bi_2Se_3. The measured temperature gradient is of around 10 K at room temperature. The temperature of close side (hot side) increases of around 15 K and the temperature of cold side increases of around 5 K. This temperature gradient is decreasing when the sample temperature decreases because the most heat generated by the Pt heater conducts through the highly thermal conductive GaAs substrate. The thermal conductivity of the GaAs is increasing when the temperature decreases, hence, the temperature gradient is decreasing. The sign

of the Seebeck coefficient ($S = -\Delta V/\Delta T$) is negative. Because the voltage of hot side is larger than the cold side, the negative charge carriers move to the cold side so that the Seebeck coefficient is negative. Hence, the Bi_2Se_3 is n-type (electron) semiconductor. The absolute values of the Seebeck coefficient are increasing when the thickness of the sample increases.

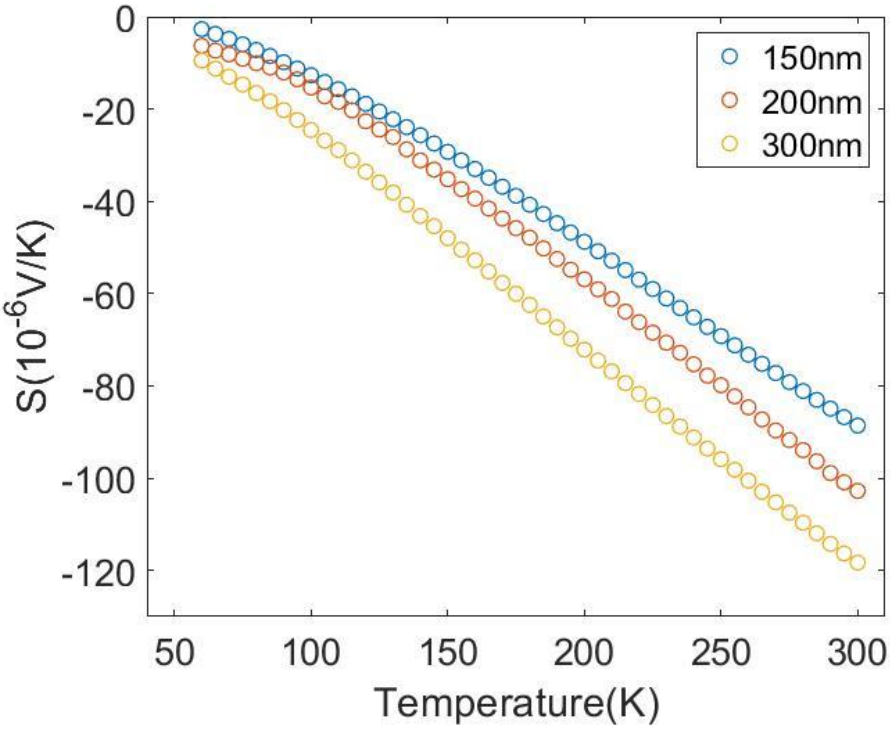

Figure 4.7 The Seebeck coefficients of Bi_2Se_3 with the temperature range of 60K – 300K.

Finally, with the Seebeck coefficient, electrical and thermal conductivities, the thermoelectric figure of merit can be calculated by $ZT = S^2\sigma T/\kappa$. As the Seebeck coefficient is near zero at low temperature, the figure of merit is also near zero. At room temperature, the ZT of 300 nm, 200 nm, and 150 nm are 0.089, 0.123,

0.074, respectively. The highest ZT is mainly due to reduced thermal conductivity and high power factor.

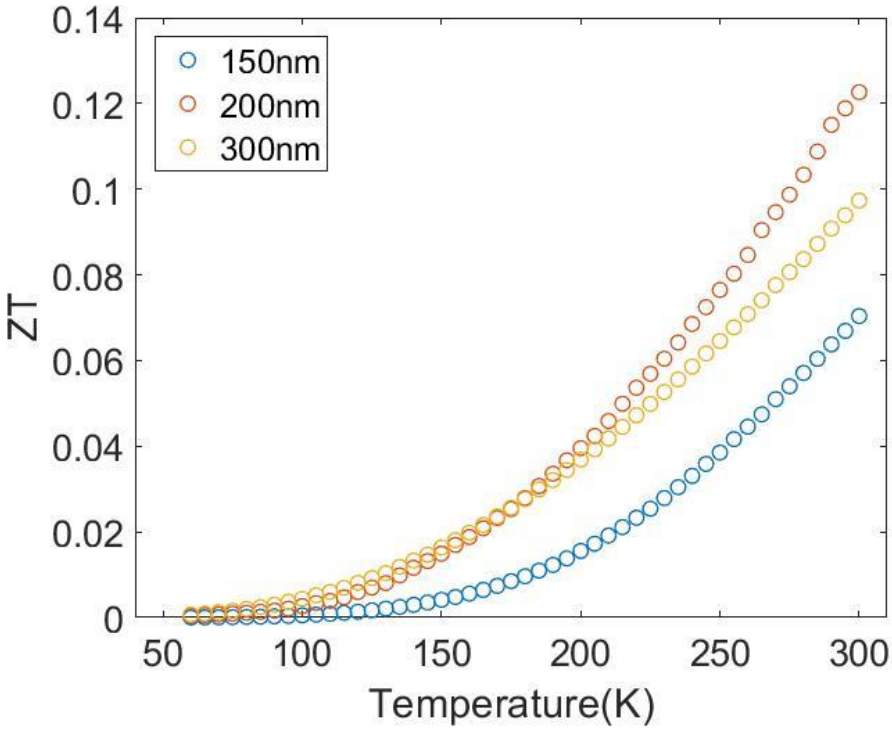

Figure 4.8 The calculated thermoelectric figure of merit of Bi_2Se_3 with the temperature range of 60K – 300K.

Chapter 5

Discussion and Conclusion

The thickness variation was conducted by 20 nm, 30 nm, 100 nm, 150 nm, 200 nm, and 300 nm. The data of 20 nm, 30 nm, and 100 nm is not presented in this report because the suspended structure is easily broken by the vibration of the compressor and even by the pressure of the rotary pump. High vacuum is needed for measuring the thermal conductivity to minimize heat diffusion to the environment, so the measurement was failed. However, the Bi_2Se_3 thinner than 150nm keep its suspended structure more than 7 days in the vibrating chamber. Hence, this dissertation can deal with the thermoelectric effect of MBE grown thin films.

The thermal conductivity is measured by the method of 3ω, thus the current sweep is needed to insure this method is applicable and calculate the value $I^3/V_{3\omega}$ from the linear fitting (Fig. 5.1). Every single point at the thermal conductivity results from the 10 times of current sweep and two points of temperature – resistance relation (5K difference). To consider the thermal time constant as zero, the frequency of AC current was set to 13 Hz that is small enough to approximate ωγ as zero. The thermal conductivities of 300 nm show that similar to the bulk Bi_2Se_3. At room

temperature, its value is 4.023 W/mK that is much higher than the 1.67 W/mK (150 nm) and 2.53 W/mK (200 nm).

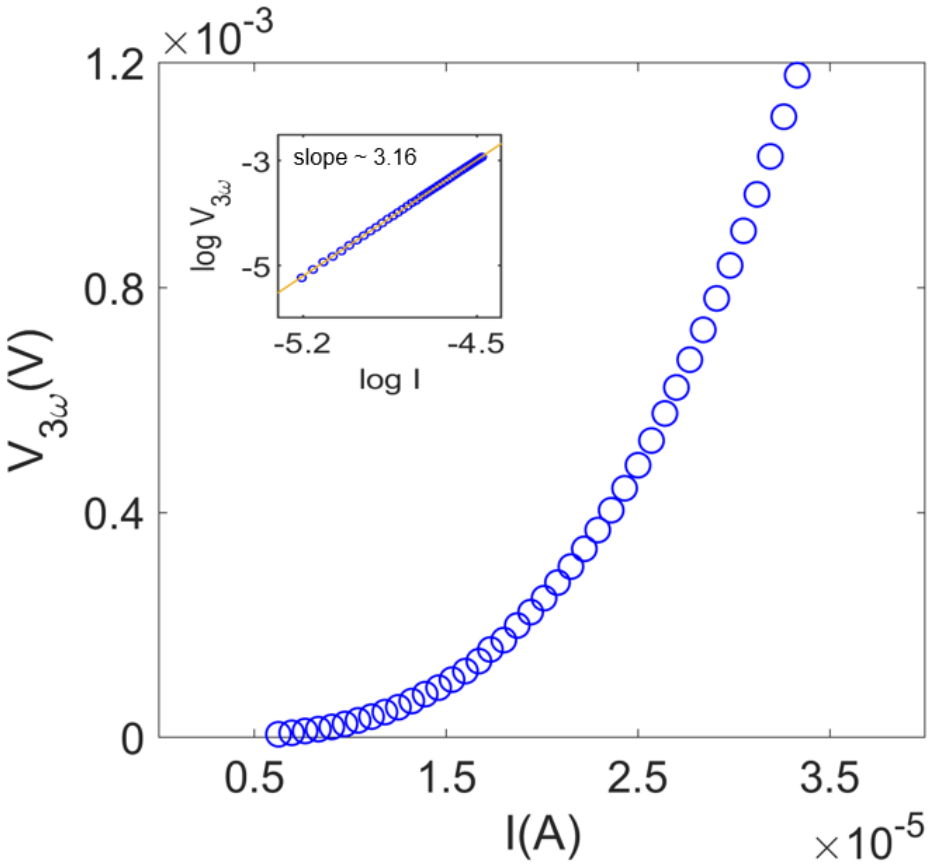

Figure 5.1 The current sweep for the 3ω method at room temperature.

The electrical conductivity is measured simultaneous with the measurement of the thermal conductivity by taking a reference signal from a lock-in amplifier and connect two lock-in voltage probes (Figure 4.5). Even the Joule's heating is not significant, the smallest value of the current during the current sweep is chosen to measure the resistance. Then, with the measured geometry, the electrical conductivity is calculated. At room temperature the highest electrical conductivity is

93659 S/m for the 300 nm thick sample. And the electrical conductivities of 150 nm and 200 nm are 49176 S/m and 75581 S/m, respectively. In the determination of the electrical conductivity and thermal conductivity, the error in the measurement of the thickness result in an error of around 5%. However, the figure of merit is $\mathrm{ZT} = S^2\sigma T/\kappa$, hence the error of the geometry is canceled out.

To exclude the voltage artifacts when determining of the Seebeck coefficient, the voltage difference was measured. When the heater is turned off, i.e., no thermal gradient, the voltage V_0 was measured. With a proper time delay after the heater is turned on, the voltage V was measured. Then the difference $V_s = V - V_0$, is taken as the value of the Seebeck voltage. The absolute value of the Seebeck coefficient is largest in the sample of 300 nm thick Bi_2Se_3. However, the Seebeck coefficient is not that different from the different thickness sample than the electrical and thermal conductivities. The Seebeck coefficients of 150 nm, 200 nm, and 300 nm sample are -91.4 μV/K, -102.8 μV/K, and -112.7 μV/K, respectively.

The figure of merit (ZT) is then calculated from the Seebeck coefficient, electrical and thermal conductivities. The calculated ZT of 150nm, 200nm, and 300nm sample are 0.074, 0.123, and 0.089, respectively at room temperature. This implies that the smaller dimensional size does not guarantee higher figure of merit. Theoretically, the thermal conductivity is more reduced than the electrical conductivity, hence smaller size is known as a key to obtain high thermoelectric

efficiency. However, due to the reduced Seebeck coefficient, the highest figure of merit is found at 200 nm thick sample.

Chapter 6

Summary

In this dissertation, the MBE growth technique is introduced to optimize the growth conditions. The growth of GaAs buffer layer is optimized by adopting the proper Ga flux (growth rate) and the thickness (growth time). With the different conditions, grown GaAs buffer layers are examined by AFM, especially the surface defects and RMS roughness. When the flux of Ga is 2.0×10^{-8} Torr and the thickness is 40 nm, the roughness is the lowest and no surface defect is scanned. This growth technique enables to control the thickness, surface morphology, and some defects. To determine the thermoelectric effect of the Bi_2Se_3, the sample is suspended from the GaAs (111)A substrate by selective wet etching. To minimize the chemical reaction between the Bi_2Se_3 and the etchant, Citric acid, the etching window (PMMA A5) is patterned at both sides of the area of Bi_2Se_3 that is to be suspended. The critical point drying prevent the suspended structure from collapse by the surface tension of

a liquid. With the incorporated Pt probes and heater, the simultaneous measurement of all the three physical quantities was possible. Even with the careful measurement, the Bi_2Se_3 thinner than 150 nm is easily broken by a vacuum pump and vibration of the chamber. Hence, this dissertation deals with 150 nm, 200 nm, and 300 nm thick Bi_2Se_3. The results indicate that the thinner Bi_2Se_3 show reduced values of Seebeck coefficient (absolute value), thermal and electrical conductivities. However, with all the three physical quantities, the resultant figure of merit is more complicated. 200 nm thick Bi_2Se_3 shows the highest figure of merit as 0.122 at room temperature. Such changes in the thermal electrical properties resulted in an increase in the figure of merit compared with the bulk of Bi_2Se_3.

Bibliography

1. Rong, G.; Zheng, Y.; Sawan, M., Energy Solutions for Wearable Sensors: A Review. *Sensors* **2021,** 21, (11), 3806.
2. Choi, H.-S.; Yun, S.; Whang, K.-i., Development of a temperature-controlled car-seat system utilizing thermoelectric device. *Applied Thermal Engineering - APPL THERM ENG* **2007,** 27, 2841-2849.
3. Zoui, M. A.; Bentouba, S.; Stocholm, J. G.; Bourouis, M., A Review on Thermoelectric Generators: Progress and Applications. *Energies* **2020,** 13, (14), 3606.
4. Goupil, C.; Seifert, W.; Zabrocki, K.; Müller, E.; Snyder, G. J., Thermodynamics of Thermoelectric Phenomena and Applications. *Entropy* **2011,** 13, (8), 1481-1517.
5. Dames, C., Cost optimization of thermoelectric materials for power generation: The case for ZT at (almost) any cost. *Scripta Materialia* **2016,** 111, 16-22.
6. DiSalvo, F. J., Thermoelectric cooling and power generation. *Science* **1999,** 285, (5428), 703-6.
7. Cutler, M.; Leavy, J. F.; Fitzpatrick, R. L., Electronic Transport in Semimetallic Cerium Sulfide. *Physical Review* **1964,** 133, (4A), A1143-A1152.

8. Snyder, G. J.; Toberer, E. S., Complex thermoelectric materials. *Nature Materials* **2008,** 7, (2), 105-114.

9. Sootsman, J. R.; Chung, D. Y.; Kanatzidis, M. G., New and old concepts in thermoelectric materials. *Angew Chem Int Ed Engl* **2009,** 48, (46), 8616-39.

10. Pei, Y.; LaLonde, A. D.; Heinz, N. A.; Shi, X.; Iwanaga, S.; Wang, H.; Chen, L.; Snyder, G. J., Stabilizing the optimal carrier concentration for high thermoelectric efficiency. *Adv Mater* **2011,** 23, (47), 5674-8.

11. Hor, Y. S.; Richardella, A.; Roushan, P.; Xia, Y.; Checkelsky, J. G.; Yazdani, A.; Hasan, M. Z.; Ong, N. P.; Cava, R. J., *p*-type Bi_2Se_3 for topological insulator and low-temperature thermoelectric applications. *Physical Review B* **2009,** 79, (19), 195208.

12. Chen, Z.-G.; Han, G.; Yang, L.; Cheng, L.; Zou, J., Nanostructured thermoelectric materials: Current research and future challenge. *Progress in Natural Science: Materials International* **2012,** 22, (6), 535-549.

13. Minnich, A. J.; Dresselhaus, M. S.; Ren, Z. F.; Chen, G., Bulk nanostructured thermoelectric materials: current research and future prospects. *Energy & Environmental Science* **2009,** 2, (5), 466-479.

14. Szczech, J. R.; Higgins, J. M.; Jin, S., Enhancement of the thermoelectric properties in nanoscale and nanostructured materials. *Journal of Materials Chemistry* **2011,** 21, (12), 4037-4055.

15. Dresselhaus, M. S.; Chen, G.; Tang, M. Y.; Yang, R. G.; Lee, H.; Wang, D. Z.; Ren, Z. F.; Fleurial, J.-P.; Gogna, P., New Directions for Low-Dimensional Thermoelectric Materials. *Advanced Materials* **2007,** 19, (8), 1043-1053.

16. Liu, T.-H.; Zhou, J.; Li, M.; Ding, Z.; Song, Q.; Liao, B.; Fu, L.; Chen, G., Electron mean-free-path filtering in Dirac material for improved thermoelectric performance. *Proceedings of the National Academy of Sciences* **2018,** 115, (5), 879-884.

17. Boukai, A. I.; Bunimovich, Y.; Tahir-Kheli, J.; Yu, J.-K.; Goddard Iii, W. A.; Heath, J. R., Silicon nanowires as efficient thermoelectric materials. *Nature* **2008,** 451, (7175), 168-171.

18. Hochbaum, A. I.; Chen, R.; Delgado, R. D.; Liang, W.; Garnett, E. C.; Najarian, M.; Majumdar, A.; Yang, P., Enhanced thermoelectric performance of rough silicon nanowires. *Nature* **2008,** 451, (7175), 163-167.

19. Harman, T. C.; Taylor, P. J.; Walsh, M. P.; LaForge, B. E., Quantum Dot Superlattice Thermoelectric Materials and Devices. *Science* **2002,** 297, (5590), 2229-2232.

20. Lin, C.-K.; Chen, M.-S.; Huang, R.-T.; Cheng, Y.-C.; Lee, P.-Y., Thermoelectric Properties of Alumina-Doped $Bi_{0.4}Sb_{1.6}Te_3$ Nanocomposites Prepared through Mechanical Alloying and Vacuum Hot Pressing. *Energies* **2015,** 8, (11), 12573-12583.

21. Alam, H.; Ramakrishna, S., A review on the enhancement of figure of merit from bulk to nano-thermoelectric materials. *Nano Energy* **2013,** 2, (2), 190-212.

22. Cahill, D. G., Thermal conductivity measurement from 30 to 750 K: the 3ω method. *Review of scientific instruments* **1990,** 61, (2), 802-808.

23. Borca-Tasciuc, T.; Kumar, A.; Chen, G., Data reduction in 3ω method for thin-film thermal conductivity determination. *Review of scientific instruments* **2001,** 72, (4), 2139-2147.

24. Dames, C.; Chen, G., 1 ω, 2 ω, and 3 ω methods for measurements of thermal properties. *Review of scientific Instruments* **2005,** 76, (12), 124902.

25. Lu, L.; Yi, W.; Zhang, D., 3ω method for specific heat and thermal conductivity measurements. *Review of scientific instruments* **2001,** 72, (7), 2996-3003.

26. Hasan, M. Z.; Kane, C. L., Colloquium: Topological insulators. *Reviews of Modern Physics* **2010,** 82, (4), 3045-3067.

27. Brahlek, M.; Lapano, J.; Lee, J. S., Topological materials by molecular beam epitaxy. *Journal of Applied Physics* **2020,** 128, 210902.

28. Ginley, T. P.; Wang, Y.; Law, S., Topological Insulator Film Growth by Molecular Beam Epitaxy: A Review. *Crystals* **2016,** 6, (11), 154.

29. Morresi, L., *Basics of Molecular Beam Epitaxy (MBE) technique*. **2013**.

30. M Franchi, S.; Trevisi, G.; Seravalli, L.; Frigeri, P., Quantum dot nanostructures and molecular beam epitaxy, S Franchi et al. In 2003.

31. Ginley, T. P.; Wang, Y.; Law, S., Topological Insulator Film Growth by Molecular Beam Epitaxy: A Review. *Crystals* **2016,** 6, (11), 154.

32. Bansal, N.; Kim, Y. S.; Edrey, E.; Brahlek, M.; Horibe, Y.; Iida, K.; Tanimura, M.; Li, G.-H.; Feng, T.; Lee, H.-D.; Gustafsson, T.; Andrei, E.; Oh, S., Epitaxial growth of topological insulator Bi_2Se_3 film on Si(111) with atomically sharp interface. *Thin Solid Films* **2011,** 520, (1), 224-229.

33. Ohtake, A.; Nakamura, J.; Komura, T.; Hanada, T.; Yao, T.; Kuramochi, H.; Ozeki, M., Surface structures of GaAs{111}*A*,*B*-(2×2). *Physical Review B* **2001,** 64, (4), 045318.

34. Bansal, N.; Kim, Y. S.; Edrey, E.; Brahlek, M.; Horibe, Y.; Iida, K.; Tanimura, M.; Li, G.-H.; Feng, T.; Lee, H.-D., Epitaxial growth of topological insulator Bi_2Se_3 film on Si (111) with atomically sharp interface. *Thin Solid Films* **2011,** 520, (1), 224-229.

35. Kraemer, D.; Chen, G., A simple differential steady-state method to measure the thermal conductivity of solid bulk materials with high accuracy. *Review of Scientific Instruments* **2014,** 85, (2), 025108.

36. Ballard, S. S.; McCarthy, K. A.; Davis, W. C., A Method for Measuring the Thermal Conductivity of Small Samples of Poorly Conducting Materials such as Optical Crystals. *Review of Scientific Instruments* **1950,** 21, (11), 905-907.

37. McCarthy, K. A.; Ballard, S. S., New Data on the Thermal Conductivity of Optical Crystals*. *J. Opt. Soc. Am.* **1951,** 41, (12), 1062-1063.

38. Stuckes, A. D., Thermal Conductivity of Indium Antimonide. *Physical Review* **1957,** 107, (2), 427-428.

39. Chiritescu, C.; Cahill, D. G.; Nguyen, N.; Johnson, D.; Bodapati, A.; Keblinski, P.; Zschack, P., Ultralow thermal conductivity in disordered, layered WSe2 crystals. *Science* **2007,** 315, (5810), 351-353.

40. Luckyanova, M. N.; Garg, J.; Esfarjani, K.; Jandl, A.; Bulsara, M. T.; Schmidt, A. J.; Minnich, A. J.; Chen, S.; Dresselhaus, M. S.; Ren, Z., Coherent phonon heat conduction in superlattices. *Science* **2012,** 338, (6109), 936-939.

41. Jiang, P.; Qian, X.; Yang, R., Tutorial: Time-domain thermoreflectance (TDTR) for thermal property characterization of bulk and thin film materials. *Journal of Applied Physics* **2018,** 124, (16), 161103.

42. Cahill, D. G.; Fischer, H. E.; Klitsner, T.; Swartz, E. T.; Pohl, R. O., Thermal conductivity of thin films: Measurements and understanding. *Journal of Vacuum Science & Technology A* **1989,** 7, (3), 1259-1266.

43. Dames, C., Measuring the thermal conductivity of thin films: 3 omega and related electrothermal methods. *Annual Review of Heat Transfer* **2013,** 16.

44. Bogner, M.; Benstetter, G.; Fu, Y. Q., RETRACTED: Cross-and in-plane thermal conductivity of AlN thin films measured using differential 3-omega method. In Elsevier: 2017.

45. Park, S. Measurement of the field-angle-dependent spin Nernst voltage across ferromagnetic probes. Ph.D. dissertation, Seoul National University, 2022.

46. Yang, C.; Lee, J.-H.; Jo, M.; Choi, H. K.; Park, S.; Kim, Y. D.; Cho, S. U.; Kim, D.; Park, Y. D., Nanomachining-enabled strain manipulation of magnetic anisotropy in the free-standing GaMnAs nanostructures. *Scientific Reports* **2019,** 9, (1), 13633.

47. Sofo, J. O.; Mahan, G. D., Optimum band gap of a thermoelectric material. *Physical Review B* **1994,** 49, (7), 4565-4570.

48. Mishra, S. K.; Satpathy, S.; Jepsen, O., Electronic structure and thermoelectric properties of bismuth telluride and bismuth selenide. *Journal of Physics: Condensed Matter* **1997,** 9, 461-470.

49. Li, G.; Liang, D.; Qiu, R. L. J.; Gao, X. P. A., Thermal conductivity measurement of individual Bi2Se3 nano-ribbon by self-heating three-ω method. *Applied Physics Letters* **2013,** 102, (4), 043104.

50. Tang, H.; Wang, X.; Xiong, Y.; Zhao, Y.; Zhang, Y.; Zhang, Y.; Yang, J.; Xu, D., Thermoelectric Characterization of Individual Bismuth Selenide Topological Insulator Nanoribbons. *Nanoscale* **2015,** 7.

51. Paulatto, L.; Fournier, D.; Marangolo, M.; Eddrief, M.; Atkinson, P.; Calandra, M., Thermal conductivity of Bi_2Se_3 from bulk to thin films: Theory and experiment. *Physical Review B* **2020,** 101.

52. Kadel, K.; Kumari, L.; Li, W. Z.; Huang, J. Y.; Provencio, P. P., Synthesis and Thermoelectric Properties of Bi_2Se_3 Nanostructures. *Nanoscale Res Lett* **2010,** 6, (1), 57.

53. Wright, D. A., Thermoelectric Properties of Bismuth Telluride and its Alloys. *Nature* **1958,** 181, (4612), 834-834.

초록

본 연구에서는 GaAs (111)A 기판에 MBE에서 성장한 Bi_2Se_3의 열전 효과를 측정하는 방법에 대해 기술한다. Bi_2Se_3 박막의 경우 기판과 접촉하여 열 확산이 쉽게 일어나 열 전도율을 정밀하게 측정하는 것에 어려움이 있다. 이를 해결하기 위해, 나노머신 기술을 통해 Bi_2Se_3 박막 아래의 GaAs를 선택적으로 에칭하여 기판과의 분리를 이루었다. 에천트로 시트르산 용액을 사용하였고, 액체의 표면 장력에 의한 현수 구조의 붕괴를 방지하기 위해 임계점 건조 기술을 사용했다. 3ω 측정 기법은 박막의 수직한 방향 성분의 열 전도율과 무관하게 수평 방향의 열 전도율을 직접 측정할 수 있다는 점에서 측정 오차가 적은 기법으로 알려져 있다. 같은 샘플에서 제벡 계수를 동시에 측정하기 위해, 백금 증착을 통해 국소적인 발열자와 백금 온도계를 증착 하고, 직류 전류에 의한 줄 열 효과로 온도 구배를 형성하고, 백금의 저항을 측정하여 국소적 온도변화를 측정했으며, 그로 인한 전위차를 측정함으로써 제벡 계수를 구해낼 수 있었다. 구조의 불안정성으로 시간에 따라 전기적 성질이 변하는 현수 구조의 특성 상 저온 유지 장치에서 제벡 계수, 열 전도율, 전기 전도율을 한번에 측정할 수 있는 소자 제작을 하여 단 기간 내 열전 성능을 계산할 수 있도록 실험을 설계하여 20K부터 400K까지 넓은 범위에서 열전 성능을 측정할 수 있었다. 연구에 보고된 측정값은 60K

에서 300K의 온도 범위에서 Bi_2Se_3 박막의 두께를 150 nm, 200 nm, 300 nm로 변화하며 열전 효과의 변화 양상을 측정했다.

본 연구에 사용된 Bi_2Se_3 박막의 MBE성장은 성장조건의 변화에 따라 AFM 분석 결과를 파라미터 스캔하여 최적의 조건을 찾았다. 우선 GaAs 버퍼층을 성장하는데, 버퍼층은 표면의 결함 및 거칠기를 결정하는 요소로 Bi_2Se_3의 성장에 중요한 역할을 한다. GaAs 버퍼층이 없는 경우와 10 nm씩 두께의 변화를 주며 버퍼층을 성장한 경우에서 AFM 분석 결과, 일반적으로 버퍼층의 두께가 두꺼워질수록 표면의 결함이 줄어들고, 거칠기가 작아지게 되었다. 두께가 40 nm 이상에서 거칠기가 0.1 nm 수준으로 낮게 나오고, 표면의 결함 또한 발견되지 않았다. 또한, Bi_2Se_3의 성장 온도 및 성장 속도에 따라 성질 분석을 해본 결과 350℃에서 성장한 경우가 삼각형 나선구조의 모양이 가장 뚜렷하게 나타났고, 표면 결함이 최소화된 성장 속도를 채택하여 박막을 성장하였다. 박막의 성장 속도는 Bi의 플럭스에 비례하는 경향을 보여준다. 그 외에 성장 온도나 Se 셀의 플럭스 비율은 성장 속도에 영향을 미치지 않는 것으로 분석되었다. 20 nm 두께부터 300 nm 두께까지의 Bi_2Se_3박막을 성장한 결과, 100 nm 두께 이하인 경우 측정과정에서 구조의 변화로 인해 열 전도율의 측정이 불가능한 상황이 되었다. 본 연구보고에서 150 nm, 200 nm, 그리고 300 nm 세 가지 두께의 샘플 측정결과가 소개되고, 두께에 따라 열전 효과의 변화양상을 비교, 분석했다. 열전 성능 지수는 200 nm 두께의 샘플에서 가장 크게 나왔다.

핵심어 : 분자선 에피택시, 비스무트 셀레나이드, 열전 효과, 3ω 측정 기법, 나노머신

학번 : 2018-21337